

UNIVERSITY OF OKLAHOMA

GRADUATE COLLEGE

**IN SITU STRESSES AND HYDRAULIC FRACTURING IN HASSI MESSAOUD
RESERVOIR, ALGERIA**

A THESIS

SUBMITTED TO THE GRADUATE FACULTY

in partial fulfillment of the requirements for the

degree of

MASTER OF SCIENCE

By

MÂAMAR KOCEÏR

Norman, Oklahoma

1999

01
THESIS
KOC
cop. 2

**IN SITU STRESSES AND HYDRAULIC FRACTURING IN HASSI MESSAOUD
RESERVOIR, ALGERIA**

A THESIS APPROVED FOR THE
SCHOOL OF PETROLEUM AND GEOLOGICAL ENGINEERING

BY



Redirection

©Copyright by MĀAMAR KOCEĪR 1999
All Rights Reserved.

Dedication

This thesis is dedicated to my parents, my sisters, and my brother for their help and support

Acknowledgements

Thanks are due to my parents, my sisters, and my brother whose emotional and financial support throughout my life made this endeavor possible.

I would like to express my sincere gratitude to my thesis advisor professor, Dr Djebbar Tiab, for his outstanding teaching, and for offering guidance throughout this work. I would also like to thank Dr. Subhash Shah and Dr. Samuel Osisanya for their advice, excellent teaching and for agreeing to serve on my advisory committee

I would also like to thank Dr J-C Roegiers and Dr T.E. Scott, Jr for their excellent teaching.

Financial support, help and contribution from SONATRACH are duly acknowledged.

Contents

Acknowledgements	v
List of Figures	ix
List of Tables	xi
Abstract	xii
Chapter 1. Introduction	1
1.1 Introduction	1
1.2 Literature Review	2
1.3 Objective of the Study	5
Chapter 2. In-Situ Stresses and Rock Properties	6
2.1 The Elastic Properties of Rocks	6
2.1.1 Static Elastic Properties	6
2.1.1.1 Young's Modulus	7
2.1.1.2 Poisson's Ratio	11
2.1.1.3 Bulk Modulus	12
2.1.1.4 Shear Modulus	13
2.1.1.5 Compressibility	14
2.1.1.6 Biot's Coefficient	16
2.1.1.7 Skempton's Pore Pressure Coefficient (B)	16
2.1.2 Dynamic Rock Properties	17
2.2 Static Versus Dynamic Properties	18
2.3 Stress Field Determination	22

2.3.1 Stress Components	22
2.3.1.1 Virgin Stresses	22
2.3.1.2 Tectonic Stresses	23
2.3.1.3 Topographical Stresses	24
2.3.1.4 Structural Stresses	25
2.3.1.5 Other Stresses	26
2.3.2 Stress Field Measurements (Orientation and Magnitudes)	26
2.3.2.1 Small Volume Hydraulic Fractures	27
2.3.2.2 Overcoring Technique	32
2.3.2.3 Core Based Measurements	32
2.3.2.4 Borehole Breakouts	34
2.3.2.5 Acoustic Emission	35
2.3.3 Importance of In-Situ Stress Orientation	36
2.4 Mechanical Properties-Logs Correlations	39
2.4.1 In-situ Stress Profiles.....	41
Chapter 3. Hydraulic fracturing in HMD	44
3.1 Reservoir Description	44
3.2 Hydraulic Fracturing in HMD	48
3.2.1 Discussion of the Results of Hydraulic Fracturing in HMD.....	49
3.2.2 Microfrac Measurements in HMD field	56
3.2.3 Discussion of the Correlations	58
3.2.3.1 Young's Modulus-Logs Correlations.....	58
3.2.3.2 Minimum Horizontal stress-Logs Correlation.....	60
3.3 In-Situ Stress Orientation in HMD.....	66

Chapter 4. Discussion of Stress Correlation Application in Hassi Messaoud	70
4.1 Application of the New Correlation	70
4.2 Comparison Between HMD Correlation and the New One	73
4.3 Sensitivity Analysis of the Correlation	74
4.4 General Considerations	76
Chapter 5. Summary, Conclusions and Recommendations	88
5.1 Summary	88
5.2 Conclusions.....	91
5.3 Recommendations	91
Nomenclature	93
References	95
Appendix	100
A.1 Review on the Wellbore	101
A.2 Log-log Stress Correlation of a Multistaging Program	107
A.3 Flow Performance after Graveling	117
A.4 Graveling Stress Transformation for a Horizontal Wellbore	121
A.5 Circumferential Stress Around a Horizontal Wellbore	127
A.6 Location of Flow Movement Field, Algeria	131
A.7 Results in 2000 Formation	135
A.8 Graveling Importance of Drilling by Layer in HMD	139
A.9 Graveling Importance of Layers and Frequency of Fracturing	143
A.10 Fracturing Importance of Zone AB	147
A.11 Fracturing Importance of Zone BC	151
A.12 Fracturing Importance of Zone CD	155
A.13 Fracturing Importance of Drilling by Layer in Zones A, B, and C	159
A.14 Fracturing Importance of Drilling by Layer in Zones D, E, and F	163

List of figures

2.1	Uniaxial Compression Test	8
2.2	Sketch of Typical Stress Strain Curves	8
2.3	Sketch of Stress Strain Curve Type I	9
2.4	Sketch of Stress Strain Curve Type II	9
2.5	Tangent Young's Modulus	10
2.6	Secant Young's Modulus	10
2.7	Sketch of Stress Strain Curve Type III	11
2.8	Deformation Associated with a Uniaxial Compression Test	12
2.9	Stress Acting on a Rock Body	23
2.10	Principal Stresses vs. Depth	24
2.11	Parallel Springs Analogy	25
2.12	Stresses Around a Wellbore	28
2.13	Typical Stress Record of a Minifracturing Report	29
2.14	Core Relaxation after Coring	33
2.15	Coordinate System Transformation for a Deviated Borehole	36
2.16	Circumferential Stresses Around a Horizontal Wellbore	37
3.1	Location of Hassi Messaoud Field, Algeria	45
3.2	Faults In HMD Structure	46
3.3	Overall Frequency of Fracturing By Layer In HMD	50
3.4	Overall Presence of Layers and Frequency of Fracturing	50
3.5	Petrophysical Properties of Zone 1B	52
3.6	Petrophysical Properties of Zone 17	52
3.7	Petrophysical Properties of Zone 19	53
3.8	Petrophysical Properties of Zone 25	53
3.9	Presence of Layers and Frequency of Fracturing in Zones 1(A, B, and C)	54
3.10	Frequency of Fracturing by Layer in Zones 1(A, B, and C)	54

3.12	Frequency of Fracturing by Layer in Zones 2(N, S, and EX)	55
3.13	Stress Profile of well A	58
3.14	Stress, Shaliness, and Porosity profiles of well A	62
3.15	Measured vs. Calculated Stresses	64
3.16	Isofracturing Gradient Map of Hassi Messaoud Structure	68
4.1	Proposed Stress Profile for Well Oml602	77
4.2	Proposed Stress Profile for Well Omn402	77
4.3	Proposed Stress Profile for Well MD440	78
4.4	Proposed Stress Profile for Well MD452	78
4.5	Proposed Stress Profile for Well Oml852	79
4.6	Proposed Stress Profile for Well MD99	79
4.7	Proposed Stress Profile for Well Omn541	80
4.8	Proposed Stress Profile for Well Omn70	80
4.9	Proposed Stress Profile for Well Omn84	81
4.10	Proposed Stress Profile for Well GS7	81
4.11	Proposed Stress Profile for Well AR22	82
4.12	Proposed Stress Profile for Well GS14	82
4.13	Stress Profile Based on HMD Correlation of Well Omn402	83
4.14	Stress Profile Based on HMD Correlation of Well MD452	83
4.15	Stress Profile Based on HMD Correlation of Well Oml852	84
4.16	Stress Profile Based on HMD Correlation of Well Omn541	84
4.17	Stress Profile Based on HMD Correlation of Well Omn70	85
4.18	Stress Profile Based on HMD Correlation of Well MD440	85
4.19	Stress Profile Based on HMD Correlation of Well MD99	86
4.20	Stress Profile Based on HMD Correlation of Well Omn84	86
4.21	Stress Sensitivity to V_{sh}	87
4.22	Stress Sensitivity to Porosity	87

List of tables

2.1	Mechanical Properties –Porosity Correlation, $M = A \text{ Exp}^{b\phi}$ (From R.A. Farquhar et al ⁴¹)	39
3.1	Reservoir Properties by Lithozone	47
3.2	Hassi Messauod Average Characteristics (From McGowen, J.M. et al ⁵⁰)	47
3.3	Microfracturing Measurements of Well A Results	56
3.4	Stress Values Calculated by Eq. 3.6 vs. Measured Stresses	63
3.5	Influence of the Fracturing Gradient on the Production Gain (From McGowen, J.M. et al ⁵⁰)	65
3.6	Screen Outs Occurrence in HMD (From McGowen, J.M. et al ⁵⁰)	66
3.7	Circumferential Stresses Around a Horizontal Borehole	69
4.1	Summary of The Results of the Application of the Obtained Correlation	72
4.2	Stress Sensitivity to V_{sh}	75
4.3	Stress Sensitivity to ϕ	75
A.1	Fracturing Gradients in HMD	101
A.2	Average Petrophysical Parameter by Layer (Zone 1B)	102
A.3	Average Petrophysical Parameter by Layer (Zone 17)	102
A.4	Average Petrophysical Parameter by Layer (Zone 19)	102
A.5	Average Petrophysical Parameter by Layer (Zone 25)	102
A.6	Summary of the Data Used in the Correlation Attempts	103
A.7	Stress Estimation for the Cited Wells	104

Abstract

Understanding the rock mechanics aspects of Hassi Messaoud (HMD) reservoir is extremely important not only for hydraulic fracturing purposes but also for planning horizontal well drilling and completion. Analysis of the data generated from the hydraulic fracturing experience in Hassi Messaoud shows that fracturing is strongly lithology dependent. The magnitude and the orientation of the stress characterize the stress field. The stress magnitude in HMD is correlated to Young's modulus and shaliness. A new correlation is proposed relating minimum horizontal stress, shaliness and porosity.

The stress field orientation in Hassi Messaoud fits that observed in other locations throughout Algeria. The maximum principal stress is in the azimuth direction between 135-140° azimuth, perpendicular to HMD anticline trend. The iso-fracturing gradient map of HMD structure confirms the compartmentalization of the reservoir into two compartments, the eastern and the western compartments, the former having, relatively, low fracturing gradients and the latter having higher fracturing gradients. The results of this study could be used in the selection of candidate wells for hydraulic fracturing as well as planning horizontal well drilling and completion.

Chapter 1

Introduction

1.1 Introduction

When a well is drilled into a hydrocarbon bearing rock, the fluids must flow through the surrounding rock and converge towards the wellbore. If the pore spaces of the rock are interconnected, then channels exist through which fluids can flow and the rock is said to be permeable. The ease with which fluid can flow through a rock determines its degree of permeability. It has high permeability if oil, gas, or water can flow easily through existing channels and low permeability if the connecting channels are very small and fluid flow is restricted, either naturally or because of formation damage (positive skin). The latter may be due to drilling fluids and particles invasion (mud and cement filtrate damage), completion, well servicing, production (non-Darcy flow effects, at high rates), enhanced oil recovery operations (scale deposition) Tiab and Donaldson¹. Impaired and low permeability formations need some form of stimulation to increase their production to an economically accepted level. Stimulation is usually performed by increasing the inflow area for fluids from the formation to the wellbore.

In limestone formations, which dissolves easily in acids, the formation is fractured open by pumping acid into it under high pressure. The acid etches away part of the walls of the fracture and conductive channels remain after the fracture has closed upon release of the pumping pressure. Through these channels the oil or gas can flow towards the wellbore more easily. In sandstone formations, which do not dissolve in acid,

propping agents are pumped to hold open the created fractures obtained by pumping special fluids (fracturing fluids) under high pressure. Fracturing is used to overcome permeability restriction problems in oil and gas reservoirs, stimulating naturally low permeability or damaged formations.

Formations with low cohesive strength are likely to experience sand and fine mobility. In fact, pore collapse; local shear can occur from excessive differential stress, leading to the increase of the effective stress, (caused by large pressure draw down). Fracture stimulation increases the effective wellbore radius and flow area, and enables the production rate to be maintained, at greater bottom hole flowing pressure, reducing the effective stress, and hence, controlling sanding. This type of fracturing is called Frac Pack technique. Frac Pack technique offers the possibility of overcoming the decrease in well productivity associated with the use of gravel pack technique for controlling fine and sand migration.

1.2 Literature Review

Warpinski et al² stated that stress contrast is the predominant factor in controlling fracture growth. They analyzed in situ experiments that were accessible by mineback to determine the parameters controlling hydraulic fracture containment in layered formations. They first designed and conducted tests to determine material property differences effects. A fracture was initiated below an interface consisting of a low modulus ash-fall tuff overlain by a much higher modulus ash-flow tuff unit.³ The immediate interface between these two units has a difference in Young's modulus of a

factor five and over a distance of 10 ft (3 m), the modulus difference increases to a factor of 15.

The mineback revealed that a fracture initiated in the, low modulus, ash-fall zone, and propagated through the interface into the higher modulus ash flow tuff. Propagation of the fracture into the high modulus layer demonstrates that a material property interface will not arrest the vertical growth of a hydraulic fracture. Nevertheless, fracture width is significantly dependent on the material property, in fact, larger widths were found in low modulus regions.

Warpinski et al² also investigated the effect of minimum in situ stresses in controlling fracture growth. Small fractures were conducted near the interface, the interpretation of which showed that, below the interface, two significant in situ stress irregularities exist, and in both cases the in-situ stress increases by a factor of two to three. The ability of the in-situ stresses to restrict fracture growth was particularly evident since several fractures remained confined between the stress peaks. Also, they noticed that fracture propagation was arrested by discontinuities (faults), and whenever a fault was crossed significant change in orientation of the created fractures occurred.

Beghou³ used Data, from four-pad caliper devices: HDT (High Resolution Dipmeter Tool), SHDT (Stratigraphic High Resolution Dipmeter Tool), and BGT (Borehole Geometry Tool), in addition to the UBI (Ultrasonic Borehole Imager), to study the Ovalization in the TIMIMOUN basin (Algeria), and found the orientation of the major horizontal stress to be 134-145°. This direction was similar to that observed in GF-2, a well located in shaly sand reservoirs of Cambrian-Ordovician age within the Ahnet basin, according to Tiab⁴.

The measurement of in-situ stress is not straightforward. However, it can be estimated from logging parameters. In situ stress profiles are generally developed by use of the three following methods (Hopkins⁵)

- Measured in-situ stresses with microfracture (small volume) and/or minifracture (large volume) tests. In Hassi Messaoud, such measurements are obtained using minifracture pump in treatments before the main treatment.
- Log-based stress profiles, calibrated to measured in-situ stress data.
- Log-based stress profiles, calibrated with analogy, core, or other data.

Because of the high cost of in-situ stress measurements, well logs are often used to estimate in-situ stress profiles. The literature provides many examples where microfracturing tests have been used, in combination with logs, to develop calibrated stress profiles for a field. Hopkins⁵ mentioned that in-situ stress profiles estimated from Lithological profiles, and calibrated to measured stresses from microfracture or minifracture tests provide good results. He illustrated this point with a Gamma ray Log correlation-based stress profile that is to be calibrated based on measured stress data and/or treatment data from comparable offset wells.

Based on microfracturing test results obtained in well A in HMD, Belhaouas et al⁶ tried to correlate the stress profile with logs. The first step was to correlate the acoustic Young's modulus with logs, from 1,727 samples in well A from a sedimentary sequence of 263 m crossing the cambrian from the top of Ri to 30 m in R3. The result was a correlation, linking dynamic Young's modulus to porosity and shaliness, with a coefficient of correlation of 0.96.

1.3 Objectives of the Study Chapter 3

The knowledge of the stress field, which is characterized by its magnitude and orientation, allows the prediction of the hydraulically induced fractures locations and azimuths which is of interest for reservoir management related operations such as EOR. It is also important in the selection of candidate wells for hydraulic fracturing to avoid excessive treating pressures, in addition to its importance for determining azimuth for horizontal drilling. The main objective of this study is to understand the mechanical properties of reservoir rock in HASSI MESSAOUD field, Algeria. Specifically to determine the impact of lithology on hydraulic fracturing using data generated from the extensive hydraulic fracturing experience and microfracturing field-testing. Another objective is the investigation of the impact of the elastic rock properties, such as Young's modulus, Poisson's ratio, and other logging determined parameters on fracture location and containment such as shaliness and porosity.

Chapter 1 discusses the objectives of this study. In chapter 2 are presented the mechanical properties of rocks, their determination and their importance in hydraulic fracturing in addition to the stress field and its determination methods. Chapter 3 deals with hydraulic fracturing and the analysis of microfracturing test results in Hassi Messaoud field, Algeria. In chapter 4, the correlations use in Hassi Messaoud is discussed and other approaches to correlate the stress field as well as the field application are highlighted. Finally, chapter 5 presents the summary, conclusions and recommendations.

Chapter 2

In-Situ Stresses and Rock Properties

2.1 The Elastic Properties of Rocks

2.1.1 Static Elastic Properties

The theory of elasticity investigates relationships between external forces applied to a body and resulting changes in its size and shape. In this theory, it is assumed that displacements are small and the body returns to its original condition after the forces are removed⁷. Applied forces and resulting deformations are described by stress – strain diagrams.

Using the stress-strain relationships, elastic constants may be determined from a specimen of the rock under load using various equipments. These constants are usually referred to as the static elastic constants. Elastic constants may also be determined using wave propagation relationships from measured elastic wave velocities; these are usually referred to as the dynamic elastic constants.

Assuming that an isotropic rock behaving in an elastic manner, then:

$$\begin{pmatrix} \sigma_1 \\ \sigma_2 \\ \sigma_3 \end{pmatrix} = \begin{pmatrix} \lambda + 2\mu & \lambda & \lambda \\ \lambda & \lambda + 2\mu & \lambda \\ \lambda & \lambda & \lambda + 2\mu \end{pmatrix} \begin{pmatrix} \epsilon_1 \\ \epsilon_2 \\ \epsilon_3 \end{pmatrix} \quad (2.1)$$

Where, λ and μ are Lamé's constants.

This relationship implies that each component of strain is a linear function of the stress components.

$$\sigma_1 = \lambda \Delta + 2\mu \varepsilon_1 \quad (2.2)$$

where,

$$\Delta = \sum_{i=1}^3 \varepsilon_i \quad (2.3)$$

2.1.1.1 Young's Modulus

Young's modulus (E) is the ratio of the axial stress to the axial strain. Hence, for a uniaxial compression test ($\sigma_2 = \sigma_3 = 0$). Using Eq.2.1 we get:

$$\left\{ \begin{aligned} \sigma_1 &= \lambda(\varepsilon_1 + \varepsilon_2 + \varepsilon_3) + 2\mu \varepsilon_1 & (2.4) \\ \sigma_2 &= \lambda(\varepsilon_1 + \varepsilon_2 + \varepsilon_3) + 2\mu \varepsilon_2 & (2.5) \\ \sigma_3 &= \lambda(\varepsilon_1 + \varepsilon_2 + \varepsilon_3) + 2\mu \varepsilon_3 & (2.6) \end{aligned} \right.$$

From Eqs.2.4, 2.5, and 2.6;

$$\varepsilon_2 = \varepsilon_3, \text{ and } 2(\mu + \lambda)\varepsilon_2 = -\lambda \varepsilon_1 \quad (2.7)$$

$$\varepsilon_2 = \varepsilon_3 = -\frac{\lambda}{2(\mu + \lambda)} \varepsilon_1 \quad (2.8)$$

From Eq.2.4

$$\sigma_1 = \left(\lambda \left(1 + \frac{-2\lambda}{2(\mu + \lambda)} \right) + 2\mu \right) \varepsilon_1 \quad (2.9)$$

$$\sigma_1 = \left(\frac{\lambda\mu}{\lambda + \mu} + 2\mu \right) \varepsilon_1 \quad (2.10)$$

$$\sigma_1 = \frac{\mu(3\lambda + 2\mu)}{\lambda + \mu} \varepsilon_1 \quad (2.11)$$

And from the definition of Young's modulus:

$$E = \frac{\mu(3\lambda + 2\mu)}{\lambda + \mu} \quad (2.12)$$

E represents the rigidity of the material under uniaxial loading. Fig. 2.1 is a representation of a rock sample sustaining uniaxial compression test as well as a typical stress-strain curve associated with such a test.

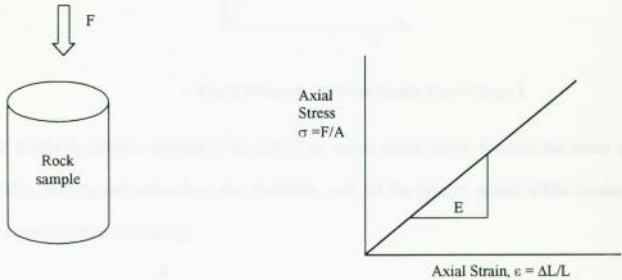


Fig. 2.1-Uniaxial Compression Test

Stress strain curves are generally not linear in actual practice, Fig.2.2 shows what normally happens during compression tests:

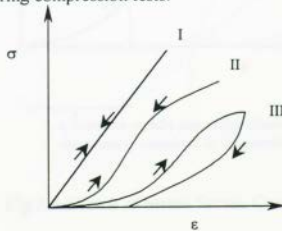


Fig. 2.2-Sketch of Typical Stress Strain Curves

I) Linear Elastic Sample (defined by a unique Young's modulus) (Fig. 2.3)

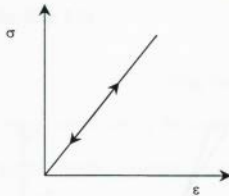


Fig. 2.3-Sketch of Stress Strain Curve Type I

II) Perfectly Elastic Sample (Fig. 2.4) The stress strain curve follows the same path while loading and unloading the specimen, and all the energy stored while loading is recovered while unloading.

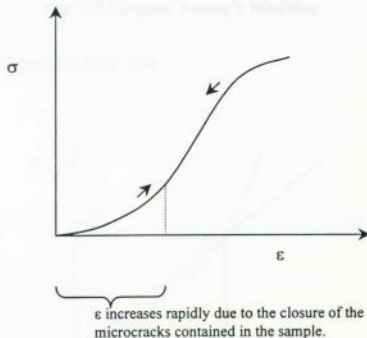


Fig 2.4-Sketch of Stress Strain Curve Type II

For such a material the elastic constants are stress dependent. Indeed two types of Young's modulus can be defined for each applied stress σ^* .

- Tangent Young's modulus (Fig. 2.5)

$$E_t = \left. \frac{d\sigma}{d\varepsilon} \right|_{\sigma=\sigma^*} \quad (2.13)$$

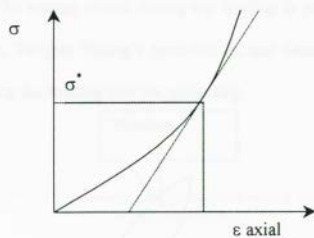


Fig. 2.5-Tangent Young's Modulus

- Secant Young's modulus (Fig. 2.6)

$$E_s = \left. \frac{\sigma}{\varepsilon} \right|_{\sigma=\sigma^*} \quad (2.14)$$

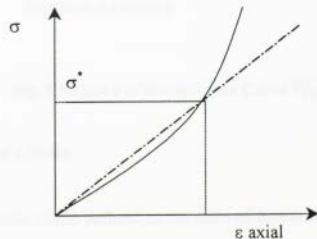


Fig. 2.6-Secant Young's Modulus

In addition another constant is introduced for classification purpose only $E_{50\%}$, which is Young's modulus calculated at a stress equal to 50% of the uniaxial compressive strength (UCS) of the rock material.

III) Visco-Elastic Material (Fig.2.7):

For such a material the path followed while loading the specimen is different from that when unloading it. The energy stored during the loading is partially dissipated during the unloading. Hence, Tangent Young's modulus, E_t , and Secant Young's modulus, E_s , will be different during the loading and the unloading.

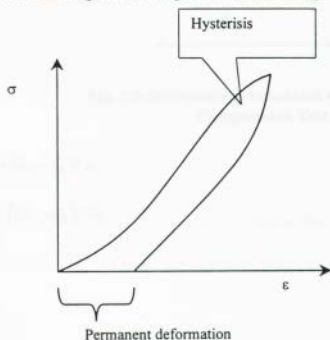


Fig. 2.7-Sketch of Stress Strain Curve Type III

2.1.1.2 Poisson's Ratio

Poisson's ratio (ν) is defined as the ratio of lateral expansion to longitudinal or axial contraction when performing a uniaxial compression test. Fig. 2.8 shows deformation (lateral and longitudinal) associated with a uniaxial compression test.

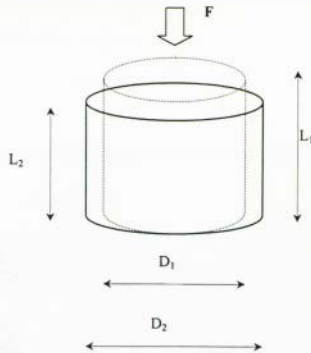


Fig. 2.8-Deformation Associated with a Uniaxial Compression Test

$$\epsilon_1 = \epsilon_{axial} = (L_1 - L_2) / L_1 \quad (2.15)$$

$$\epsilon_2 = \epsilon_{circ} = (D_1 - D_2) / D_1 \quad (2.16)$$

$$\nu = \frac{-\epsilon_2}{\epsilon_1} \quad (2.17)$$

$$\nu = \frac{\lambda}{2(\lambda + \mu)} \quad (2.18)$$

ν represents the capability of the material to transfer its deformability perpendicularly to the loading.

2.1.1.3 Bulk Modulus

The Bulk modulus (K) which is obtained using a hydrostatic test ($\sigma_1 = \sigma_2 = \sigma_3 = P$), is the ratio of the applied hydrostatic pressure to the volumetric strain produced.

$$K = \frac{P}{\Delta} \quad (2.19)$$

$$K = \frac{\sum_{i=1}^3 \sigma_i}{3\Delta} \quad (2.20)$$

Where:

$$\Delta = \sum \varepsilon_i \quad (2.21)$$

$$K = \frac{\sum \lambda \Delta + \sum 2\mu \varepsilon_i}{3 \sum \varepsilon_i}, \quad (2.22)$$

$$K = \frac{3\lambda \sum \varepsilon_i + 2\mu \sum \varepsilon_i}{3 \sum \varepsilon_i} \quad (2.23)$$

Hence,

$$K = \lambda + \frac{2}{3}\mu \quad (2.24)$$

Combining Eqs. 2.18 and 2.24 it can be shown that The Bulk modulus is related to Young's modulus and Poisson's ratio as follows:

$$K = \frac{E}{3(1-2\nu)} \quad (2.25)$$

2.1.1.4 Shear Modulus

Shear modulus (G) is a measure of a rock sample's resistance to shear stress; it is the ratio of shear stress to shear strain.

$$G = (\text{shear stress/shear strain}) = \frac{\tau_x}{\gamma_x} \quad (2.26)$$

G is equivalent to the second Lamé's constant, μ .

The Shear modulus can be calculated from Young's modulus and Poisson's ratio (Indirect measurement).

$$G = \frac{E}{2(1+\nu)} \quad (2.27)$$

It can also be related to Lamé's constant (λ) and bulk modulus (K).

$$G = \frac{3(K - \lambda)}{2} \quad (2.28)$$

λ is calculated from Young's modulus and Poisson's ratio by

$$\lambda = \frac{E\nu}{(1+\nu)(1-2\nu)} \quad (2.29)$$

The Shear modulus is not affected by the pore fluid since the shear strength of all fluids is zero.

2.1.1.5 Compressibility

Compressibility (β) is defined as the inverse of the bulk modulus, K.

$$\beta = \frac{1}{K} = \frac{3}{3\lambda + 2\mu} \quad (2.30)$$

Expressed as a function of Young's modulus, E, and Poisson's ratio, ν , compressibility could be expressed by the following expression:

$$\beta = \frac{3(1-2\nu)}{E} \quad (2.31)$$

There are three types of compressibility: bulk compressibility, rock matrix compressibility, and pore volume compressibility. These are defined based on changes in bulk volume, solid rock grain, and pore volume with respect to pressure, respectively.

Compressibility is an important parameter in the estimation of the reserves. In fact, the oil in place estimated from pressure decline data in a volumetric under-saturated reservoir, expressed in stock tank barrels (STB), is:

$$N = \frac{N_p B_o}{\beta_e \Delta P B_{oi}} \quad (2.32)$$

Where, N = initial oil in place, STB

N_p = oil production during the pressure decline, STB

B_o and B_{oi} = oil formation factors at reservoir pressure P and P_i , RB/STB

β_e = effective compressibility of the reservoir expressed as: $\beta_e = \frac{\beta_t}{S_o}$, psi^{-1}

β_t = total system compressibility expressed as:

$$\beta_t = \beta_o S_o + \beta_g S_g + \beta_w S_w + \beta_f,$$

$\beta_o, \beta_g, \beta_w, \beta_f$ = oil, gas, water, and pore compressibility, psi^{-1}

s_o, s_g, s_w = oil, gas, water saturation, and

$$\Delta P = p_i - p$$

Terzaghi⁸, noted that the increase in external confining pressure produces the same volumetric strain change as reducing the pore pressure by the same amount, and that the shear strength depends on the difference between the applied stress and pore pressure. Hence, he introduced the effective stress concept for one-dimensional consolidation and proposed the following relationship:

$$\sigma_{eff} = \sigma - P_p. \quad (2.33)$$

where, σ is the total applied stress and P_p is the pore pressure. The concept of effective stress is also essential for interpreting phenomena associated with reservoir production

such as water injection-induced shear fracturing, reservoir subsidence, and sand production.

2.1.1.6 Biot's Coefficient

Biot⁹ introduced the parameter α in the pore pressure term to account for the coupled diffusion/deformation process and introduced the modified effective stress law:

$$\sigma_{eff} = \sigma - \alpha P_p \quad (2.34)$$

α is a correction factor to pore pressure term. It corrects the cementation effects since the cementation of a rock counteracts some of the applied stress. For soils and poorly consolidated rocks α is, generally, equal to one.

2.1.1.7 Skempton's Pore Pressure Coefficient (B)

Skempton's pore pressure coefficient (B) is obtained using a hydrostatic undrained test. It is the ratio of change in pore fluid pressure to the change in external confining pressure:

$$B = \frac{\Delta P_p}{\Delta P_c} \quad (2.35)$$

A drained test is a test where fluid can escape from rock pores, which is not the case for the undrained test. At low confining pressures, generally, $B = 1$; while at high confining pressures, generally, $B < 1$.

2.1.2 Dynamic Rock Properties

Dynamic measurements require applying non-destructive loads, by propagating elastic waves, to a rock sample. In general, dynamic rock properties are different from the static properties. The difference could be attributed to the presence of microcracks constituting soft inclusions which may lower the stiffness of the rock once loaded. Depending on the wave length of the incident waves, these inclusions may or may not be seen. Hence, provide moduli closer to the intact material ones.

Cheng and Johnston¹⁰ showed that for rocks containing cracks, (sandstones, the Westerly granite, and the Ammonia Tanks Tuff), the K_s/K_d ratio, (the ratio of static and dynamic bulk moduli), is lowest at atmospheric pressure where all the cracks are open. As the pressure increases the thin cracks start to close and reduce in number, and the ratio between static and dynamic bulk moduli begins to increase. At high pressures most of the cracks are closed and the two Moduli are roughly equal in magnitude. On the other hand, for the Colorado Oil Shale with no measurable crack porosity, the K_s/K_d ratio remains relatively constant over the entire pressure range under investigation (0 – 2.25 Kilobars).

Such explanation is confirmed by the fact that, at high confining pressures, the difference between the dynamic and static measurements narrows. The dynamic elastic constants are expressed as functions of P- and S- wave velocities as the following:

$$E_d = \frac{\rho_b V_s^2 (3V_p^2 - 4V_s^2)}{V_p^2 - V_s^2} = 2\mu(1 + \nu_d) \quad (2.36)$$

$$\mu_d = G_d = \rho V_s^2 = \frac{\rho_b}{t_s^2} a \quad (2.37)$$

$$\nu_d = \frac{V_p^2 - 2V_s^2}{2(V_p^2 - V_s^2)} = \frac{\frac{1}{2}\left(\frac{t_s}{t_c}\right)^2 - 1}{\left(\frac{t_s}{t_c}\right)^2 - 1} \quad (2.38)$$

$$K_d = \rho_b \left(\frac{1}{t_c^2} - \frac{4}{3t_s^2} \right) a \quad (2.39)$$

where: ρ_b = bulk density, in g/cm³,

ν_d = dynamic Poisson's ratio,

$G_d = \mu_d$ = dynamic shear modulus, in psi,

E_d = dynamic Young's modulus, in psi,

K_d = dynamic bulk modulus, in psi,

t_c = compressional transit time, in $\mu\text{sec}/\text{ft}$,

t_s = shear transit time, in $\mu\text{sec}/\text{ft}$,

a = conversion factor = $1.34 \cdot 10^{10}$,

V_p = velocity of the compressional wave, and

V_s = velocity of the shear wave.

2.2 Static Versus Dynamic Properties

It has been reported in the literature that dynamic moduli (Young's, shear, and bulk) are higher than the static values, while for dynamic and static Poisson's ratio there is less consistency in the correlations.

Some explanations have been proposed by some authors^{11, 12, 13, 14, 15, 16}.


(a) Viscoelastic Behavior (Liquid Saturation Effects):

Yale and Jamieson¹¹ argued that part of the difference between static and Dynamic log derived mechanical properties is due to the fact that compressional velocities are higher in a fully liquid saturated rock than in a gas saturated rock. This higher compressional velocity is due to the pore fluid supporting part of the load as the wave passes ("undrained" conditions). On the other hand the frequency of the static measurements is such that pore fluid can move away from the stressed zone and does not support any of the load, even in fully liquid saturated case ("drained" conditions).

(b) Loading Conditions (Strain Amplitude and Frequency Differences):

Hilbert et al.¹² conducted two types of static loading tests: uniaxial stress tests and uniaxial strain tests. dynamic pulse transmission tests were also conducted concurrently with the static loading tests. "major" stress cycles were performed during which "minor" stress cycles were executed with small amplitudes. They noticed that the major stress strain cycles exhibit considerable hysteresis, while little hysteresis was observed in the minor stress strain cycles. In addition the velocity data exhibit a dependence on loading direction. They, also, noticed that the uniaxial stress curve has the lowest stiffness and the dynamic curve has the highest stiffness. The stiffness of the rock (Berea Sandstone) was higher in the uniaxial strain test, compared to that in the uniaxial stress test. Radial deformation was prohibited in the former leading to higher resistance of the rock sample, hence, a higher stiffness.

In the ultrasonic pulse tests of Hilbert et al¹² strain amplitude was less than 10^{-6} . Mavko¹³ has shown that this amplitude is the threshold above which attenuation occurs



due to frictional sliding between microcracks. Hence, deformation during the passage of a strain wave results only from elastic response of grains with no frictional sliding involved. The stiffness reflected in the dynamic stress strain relationship is a function of only the properties of the porous structure (skeleton), which has a higher stiffness than that which include an additional component due to frictional sliding.

It is probably impossible to accurately measure static properties at acoustic strain amplitudes (10^{-5} to 10^{-6} strain). However, at small strain, small stress amplitude cycles executed during a static uniaxial strain test, Hilbert et al¹² found the tangent moduli to match with measured dynamic moduli. Therefore, the difference between dynamic and static moduli could be, in reality, less than what it is thought to be since field deformations occur under static uniaxial strain conditions. Moreover, the moduli from the unloading portion of the static major stress cycle, at high axial stresses, match the dynamic values, indicating that the static unloading response occurs with no frictional sliding involved. During the loading phase of the major stress cycle, strains are large enough so that eventually frictional sliding occurs between microcracks. However, when the axial load is reversed during the unloading cycle the grains are 'locked' in place until the axial load is reduced to the point at which the elastic response of the grains is sufficient to overcome the frictional resistance between the grains.

For Poisson's ratio, it was found that the values calculated from the minor stress cycles agree with that calculated from the major stress strain curve during the unloading path confirming the hypothesis of no frictional sliding on microcracks.

(c) Polona and Cook¹⁴ have shown that for sandstones static Young's moduli, when consistently defined in terms of small amplitude minor cycle load- unload paths, are similar to dynamic Young's moduli, measured along the stressed direction. They, also, attributed the importance of the dynamic moduli values to the absence of frictional sliding. The static strain amplitudes (10^{-2} to 10^{-3}) are much larger than the acoustic strain amplitudes (10^{-5} to 10^{-6} strain), and, therefore, more likely to cause frictional sliding.

To show the dependence of static moduli on strain amplitude and stress in sandstones and Limestones, with a wide range of porosities and permeabilities, Tutuncu et al¹⁵ conducted a series of uniaxial stress cycling experiments on dry Berea, Bandera, Boise, Ohio and Pecos sandstones, Carthage, Leuders and Glen Rose limestones and Austin Chalk. They concluded that static moduli are strong functions of strain amplitude and stress, in sandstones and limestones. As strain amplitude increases, static Young's moduli decrease, whereas static Poisson's ratios increase.

Among the explanations for dynamic and static measurement differences is the confining pressure. In fact, at high confining pressures, the difference between the dynamic and static measurements narrows and the moduli approach an asymptotic value as the confining pressure increases, closing properly oriented cracks. The asymptotic values of Young's, bulk, and shear static moduli approach the dynamic values. In addition, measurement frequency differences (10^6 Hz vs. 10^2 Hz) and the presence of clays could explain some of the difference between the static and dynamic measurements.

In sedimentary rocks the direction of the measurements of rock properties relative to the bedding plane, in fact, Rahn¹⁶ showed that moduli of elasticity of a foliated rock can vary by about 50% if measured normally and parallel to the bedding plane. Hence, since the mechanical properties are directional, the measurements should take into account the orientation of the core with respect to the bedding plane.

2.3 Stress Field Determination

2.3.1 Stress Components

The stresses acting within the rock can be defined by three perpendicular components called principal stresses.

- One is vertical, due the overburden load, referred to as σ_v .
- The other two principal stresses are horizontal, referred to as $\sigma_{h, \min}$, $\sigma_{H, \max}$.

The actual state of stress field acting on a rock is a synthesis of several components of different origins.

2.3.1.1 Virgin Stresses

Fig. 2.9 is a representation of virgin stresses acting on a rock body

Vertical Stress

Due to the weight of the overburden, Vertical stress increases with depth. Its magnitude, at a given depth, H, is given by:

$$\sigma_v = \int_0^H \rho(Z)gdZ \quad (2.40)$$

Where, ρ is the density of the overlying rock masses and g is the acceleration of gravity. σ_v may be obtained from the integration of a density log, or it may be approximated using a stress gradient of 1.0 to 1.2 psi/ft (Fig. 2.10).

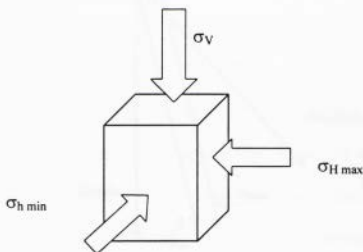


Fig. 2.9-Stresses Acting on a Rock Body

Horizontal Stresses:

The overburden load results in associated horizontal stress components, whose magnitudes depend on the lateral boundary conditions. In a basin not subjected to tectonic forces, the horizontal stress components, $\sigma_{H \max}$ and $\sigma_{h \min}$, will have the same magnitude in every direction.

2.3.1.2 Tectonic Stresses

In situ stresses are affected by the tectonic processes, which result from large crustal movements creating an additional stress component that can be vectorially added

to the virgin stress components. The influence of these tectonic forces leads to a situation where the two horizontal components are unequal.

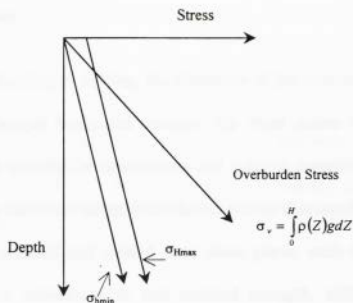


Fig. 2.10-Principal Stresses vs. Depth

The horizontal stress in the tectonic direction can be written as follows:

$$\sigma_h = \frac{\nu}{1-\nu} \sigma_v + \epsilon_T E \quad (2.41)$$

where, ϵ_T is proportional to the regional tectonic displacement.

2.3.1.3 Topographical Stresses

Surface irregularities may greatly influence the local stress field. In general, in situations where the topography is significant, the computed overburden

($\sigma_v = \int_0^H \rho(Z)gdZ$) will not be the same as the true vertical stress. For instance, in a

borehole located on a valley floor, the true vertical stress increases with depth at a greater rate than the overburden because of loading by the surrounding topography.

2.3.1.4 Structural Stresses

In the vicinity of faulting or folding, the directions of the tectonic forces control the directions of the principal horizontal stresses. Far from active tectonics, stress effects are, still felt, and usually the orientations and relative magnitudes of the two horizontal stresses can be estimated using methods that will be discussed later.

Stresses may be reduced and rotated near shear plane, such as thrust faults, because of the difference between peak and residual strength. stiffness variations between various ground strata in combination with loading history may result in stress concentration in stiff layers such as clayey shales. In fact, rock strata could be compared to a series of parallel springs, the stiffness of which are proportional to the rocks Young's moduli. The application of a constant displacement at one end leads to larger stresses in the stiffest layers¹⁷ (Fig. 2.11).

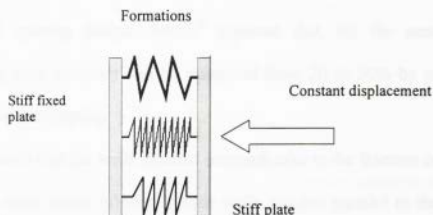


Fig. 2.11-Parallel Springs Analogy

2.3.1.5 Other Stresses

Some rocks have the property to flow or creep as soon as they are subjected to a differential stress. Salts and potashes are examples of such rocks. In this case, generally the three principal stress components are, nearly, equal. In addition, thermally induced stresses will affect the stress regime. The high horizontal stresses may be influenced by paleo-stresses generated by the overlaying earth and ice that have been removed, considering that rock seems to have a memory of previous loading. Such an effect is called fossilized stress effect.

2.3.2 Stress Field Measurements (Orientation and Magnitude)

Stress field determination is important for the oil and gas industry. In fact, many oil and gas production, completion, and reservoir engineering activities depend on the distribution of in situ stresses. It has been reported in the literature that the knowledge of the orientation of propped fractures is important to long term recovery from tight gas sands, and for well spacing design. Smith¹⁸ reported that, for the same capital investment cost, long term recovery can be improved from 20 to 50% by preventing drainage patterns from overlapping.

Dyes et al¹⁹ noted that the wells situated perpendicular to the fracture orientation will achieve a better areal sweep efficiency than wells situated parallel to the fracture direction. Other examples of the importance of stress determination are; Hydraulic fracture growth (fracture containment), proppant selection (size and type), safety and well equipment integrity concerns while fracturing, wellbore stability, sand production,

and reservoir deformation associated with production (compaction, subsidence, injection shear induced fracturing).

Several measurements methods have been reported in the literature and comparisons of the obtained results were published (Warpinski and Teufel²⁰, Teufel et al²¹, Lacy²², Smith et al²³, Oikawa et al²⁴, Masuki and K. Takeuchi²⁵, Ren and Hudson²⁶). These methods are discussed next:

2.3.2.1 Small Volume Hydraulic Fractures (Mini Hydraulic and Micro Fracturing)

Theoretical Background

If one assumes that the rock remains linear elastic, and that the borehole is drilled parallel to a direction of principal stress, the following expressions can be obtained for the near borehole induced stresses:

The stress-field, at any r and θ , is:

$$\left\{ \begin{array}{l} \sigma_{rr} = \frac{1}{2}(\sigma_x + \sigma_y) \left(1 - \frac{a^2}{r^2}\right) + \frac{1}{2}(\sigma_y - \sigma_x) \left(1 - \frac{4a^2}{r^2} + \frac{3a^4}{r^4}\right) \cos 2\theta + P \left(\frac{a^2}{r^2}\right) \end{array} \right. \quad (2.42)$$

$$\left\{ \begin{array}{l} \sigma_{\theta\theta} = \frac{1}{2}(\sigma_x + \sigma_y) \left(1 + \frac{a^2}{r^2}\right) - \frac{1}{2}(\sigma_y - \sigma_x) \left(1 + \frac{3a^4}{r^4}\right) \cos 2\theta + P \left(\frac{a^2}{r^2}\right) \end{array} \right. \quad (2.43)$$

$$\left\{ \begin{array}{l} \tau_{r\theta} = -\frac{1}{2}(\sigma_y - \sigma_x) \left(1 + \frac{2a^2}{r^2} - \frac{3a^4}{r^4}\right) \sin 2\theta \end{array} \right. \quad (2.44)$$

where, $\sigma_x = \sigma_{h, \min}$ (least principal stress), and $\sigma_y = \sigma_{H, \max}$ (maximum principal stress).

At the borehole wall ($r = a$)

$$\left\{ \begin{array}{l} \sigma_{rr} = P \\ \sigma_{\theta\theta} = (\sigma_x + \sigma_y) - 2(\sigma_y - \sigma_x) \cos 2\theta \\ \tau_{r\theta} = 0 \end{array} \right. \quad (2.45)$$

$\sigma_{\theta\theta}$ takes its minimum value at the points where $\theta = 0$ and $\theta = \pi$, and its maximum value at the points where $\theta = \pi/2$ and $\theta = 2\pi/3$. as shown in Fig. 2.12.

$$\sigma_{\theta\theta, \min} = 3\sigma_x - \sigma_y - P \quad (2.46)$$

$$\sigma_{\theta\theta, \max} = 3\sigma_y - \sigma_x - P \quad (2.47)$$

The condition for a fracture to occur is that at the points where $\sigma_{\theta\theta}$ is minimum is:

$$\sigma_{\theta\theta} = -T_0$$

or,

$$3\sigma_x - \sigma_y - P_b = -T_0 \quad (2.48)$$

$$3\sigma_{h, \min} - \sigma_{H, \max} - P_b = -T_0 \quad (2.49)$$

where: $-T_0$ is the Tensile strength of the rock, and P_b is the breakdown pressure.

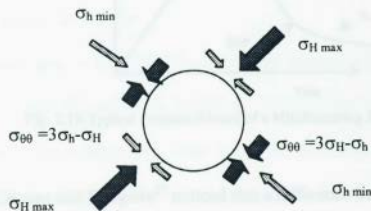


Fig. 2.12-Stresses Around a Wellbore

Induced fractures will propagate in a plane perpendicular to $\sigma_{h, \min}$ (least principal stress). It should be noted that the borehole-induced stresses diminish rapidly to zero, with increasing distances from the wellbore. Consequently, they influence only

the magnitude of the pressure required to induce a fracture, but not that required for propagating it away from the wellbore wall.

Procedure

Minifracuring consists of sealing off an open hole section with straddle packers, pressurizing it until failure, the injection is stopped and the instantaneous shut in pressure (ISIP) is determined (pressure is recorded continuously). Fig. 2.13 is a sketch of a typical pressure record obtained during a minifracuring test. It is to be pointed out that for this small treatment, with low viscosity fluid, ISIP is essentially equal to the minimum principal in situ stress.

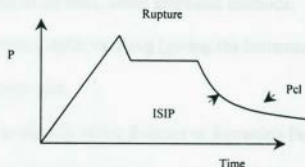


Fig. 2.13-Typical Pressure Record of a Minifracuring Report

McLennan and Roegiers²⁷ noticed that a difference between microfracturing and minifracuring does exist. They stated that there is an order or two of magnitude difference in fluid quantities between them. Microfracturing field testing cases has been reported in the literature. Sarda et al²⁸ conducted microfracturing tests on three wells situated in Northwest Europe. They determined that stress contrasts exist between permeable zones and other non-permeable zones, considered as stress barriers. They also noticed that the exploitation of reservoir influences the stress contrast between the

reservoirs and the impermeable barriers. In fact, reservoir production makes the stress contrast go up. In addition, Tinker et al²⁹ by analyzing the microfracs, successfully conducted in the Grayburg/San Andres formations at the Waddell Field in Crane County, Texas, noticed variations in stress across the field. They attributed this differences in reservoir pressure. In this paper, the authors recommended microfrac tests to prevent vertical fracture extension.

Data Analysis

Several interpretation methods for predicting minimum principal stress from pressure records have been investigated in the literature, Proskin et al³⁰ analyzed a series of minifracs, performed in oil sand, using graphical methods:

- 1 Pressure derivative plot, dp/dt vs. P_{avg} (giving the Instantaneous Shut In Pressure).
- 2 P vs. $\text{Log}(t_{inj} + \Delta t)/\Delta t$ plot.
- 3 Square root time, to identify either fracture or formation linear flow.
- 4 Tandem square root plot (P vs. $\text{SQRT}(t_{inj} + \Delta t) - \text{SQRT}(\Delta t)$).

The methods yield to reasonably close values for minimum principal stress except for the ISIP method. Several factors complicating the interpretations of pressure decay records exist:

- Leak off, especially in permeable formations, the recorded stress level is, probably, pore pressure dependent.
- Fracture inclination and change in fracture propagation direction.

- In situ stress heterogeneities: During fracture propagation, it is likely that the fracture extends into other zones of different stress levels, and these zones must be reflected in the shut in pressure response.
- Incomplete fracture closure.

G function Plot: (Castillo³¹)

The basic decline analysis requires the slope of a straight line from the G- plot of p_w vs. G.

Considering fluid loss dominated case (Lower bound):

$$G(\Delta t_D) = \frac{4}{\pi} \left[(1 + \Delta t_D) \sin^{-1} (1 + \Delta t_D)^{-\frac{1}{2}} + \Delta t_D^{\frac{1}{2}} - \frac{\pi}{2} \right] \quad (2.50)$$

Considering the minimum fluid loss case (Upper case):

$$G(\Delta t_D) = \frac{16}{3\pi} \left[(1 + \Delta t_D)^{\frac{3}{2}} - \Delta t_D^{\frac{3}{2}} - 1 \right] \quad (2.51)$$

where: t_D = the dimensionless shut in time,

$$t_D = \frac{t}{t_p} - 1 \quad (2.52)$$

t = time since start of pumping, and

t_p = the pumping time.

Instantaneous Shut In Pressure is the pressure occurring immediately after shut in. It is alleged that this is the final propagation pressure minus the friction pressure, and it corresponds to the equilibrium state after shut in. Fracture closure pressure is defined as the pressure required to keep the fracture from just closing. It is taken to represent the minimum horizontal stress. However, researchers Nolte and Smith³², McLennan and

Roegiers²⁷, noticed that closure pressure manifests a total stress localized around the fracture and does not reflect the far field principal stress.

2.3.2.2 Overcoring Technique

Overcoring methods rely on the fact that a rock core, when drilled, is relieved of most in situ stress and expand to its initial unstressed state. Stress relief is usually measured by inserting a strain measuring device or a diameter gauge into a small pilot hole. Initial readings are recorded and a concentric hole, of large diameter, is drilled. The annulus of core that contains the stress meter is then removed. The original stress may be estimated by applying an external stress to the core until the stress meter registers its initial values.

2.3.2.3 Core Based Measurements

Anelastic Strain Recovery (ASR)

Teufel³³ developed a technique for determining the strain relief direction on freshly cut oriented cores. The ASR technique Warpinski and Teufel³⁴ consists of mounting clip on displacement gauges on a piece of sealed, oriented core and recording the time dependent relaxation of that core, in a temperature controlled environment. Determination of the stress field orientation has been shown to be straight forward, for many sedimentary rocks and is readily determined by knowing the principal strain orientation. If there is no rock fabric to distort the results, the maximum stress direction is found to be coincident with the maximum strain direction.

Microcrack Model

Teufel³³ has proposed a microcrack model of stress relaxation. Upon coring the in situ stresses are released and the rock is allowed to expand in all directions (Fig. 2.14). Because the X direction has suffered the greatest stress release, it will expand the most inducing lot of cracks. The Y direction is least cracked since it has suffered the least amount of stress release.

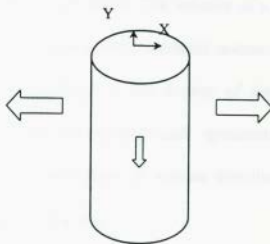


Fig. 2.14-Core Relaxation After Coring

Differential Strain Curve Analysis (DSCA)

DSCA, defined by Smith et al²³, is a technique for determining the spatial orientation of the principal stresses. It is based on the assumption that oriented microcracks were induced in the core sample, by the stress relief, when it was taken out from depth, and their density is proportional to the relieved stress magnitudes. Hence, when a core sample is hydrostatically compressed, the differential strains are observed along various directions, related to in-situ- stress state. Also, the deformation behavior

of the sample is, mainly, affected by the stress relief-induced microcracks, the effects of pre-existing and thermally induced cracks are small and can be neglected.

Differential Wave Velocity Analysis (DWVA)

DWVA is used to determine the spatial orientation as well as the ratio of the principal stress components. It is based on the same assumptions as DSCA (microcracking), and the analysis is similar, except that compressional acoustic wave velocity is measured rather than strain. The velocity of a compressional wave in a rock specimen will decrease if appropriately oriented microcracks exist, and the degree of velocity variation is proportional to the density of the microcracking in a specific direction. Therefore, when an oriented rock specimen is submitted to hydrostatic reloading, wave velocity observation, in various directions, is an indicator of the pre-existing downhole stress conditions.

2.3.2.4 Borehole Breakouts (Ovalization)

Wellbore breakouts result from the elongation of the borehole, forming intervals with non-circular cross section whose long axis is parallel to the minimum horizontal stress direction. Hence, Ovalization is an indicator of the direction of the horizontal principal stress. Tools for determining borehole breakouts are: borehole viewers and oriented calipers. Several cases where wellbore breakout analysis has been a successful means for stress direction detection are encountered in the literature.

Teufel et al²¹ compared the hydraulic fracture azimuth determined by breakouts and by several other techniques, at the Multi Well Experiment site, near Rifle,

Colorado, and found an agreement with the oriented core analysis. Shamir and Zoback³⁵ presented based on stress induced wellbore breakout and ultrasonic televiewer a detailed profile of the direction of $\sigma_{H \max}$ in the Cajon pass, California. Also Vernic and Zoback³⁶ reported the applicability of wellbore breakout analysis as well as Differential Wave Velocity Analysis for the estimation of in situ stress at great depths exceeding 10 Km.

Failure Mechanisms of Borehole Breakouts

Lee and Haimson³⁷ conducted a laboratory study on thin sections of borehole breakouts on Lac Du Bonnet Granite. They found that the governing mechanism of borehole breakouts is stress induced extensile cracking in the two zones aligned with σ_{hmin} direction.

2.3.2.5 Acoustic Emission-Kaiser Effect

The Kaiser effect is a sudden increase in the rate of acoustic emission that occurs when the applied stress has reached a level greater than the previously applied to the rock specimen. The Kaiser effect was investigated by several authors, and its reliability was proven. Recently, Seto et al³⁸ conducted a study to measure in situ rock stress using the Kaiser effect, on cores obtained from three different kinds of vertically drilled exploratory boreholes and one horizontally drilled borehole in an underground coal mine, with time lags up to 2 years. The results of these measurements were compared with results obtained from over coring and hydraulic fracturing techniques. Michihiro et al³⁹ studied whether the Kaiser effect is affected by initial geo-stress and

concluded that the stress estimated from the Kaiser effect is equal to the stress which presently causes strain in specimens and not the largest stresses they have sustained in the past.

2.3.3 Importance of In-Situ Stress Orientation

Stress field orientation knowledge is of importance for reservoir related design concerns such as hydraulic fractures azimuths, borehole stability horizontal drilling and completion planning. In fact, for a horizontal section to be drilled in a horizontal well the worst orientation to be selected, in the case where the overburden stress is highest of principal stresses, is parallel to the maximum horizontal stress.

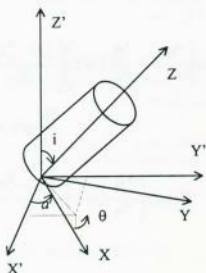


Fig .2.15-Coordinate System Transformation For a Deviated Borehole⁴⁰

Figure 2.15 represents coordinates system transformation for a deviated borehole. The angle a represents the azimuth angle, and the angle i represents the wellbore deviation (inclination) The stresses around a wellbore are given by the

following general linear elastic solution assuming no displacement along the z- axis (plane strain condition):

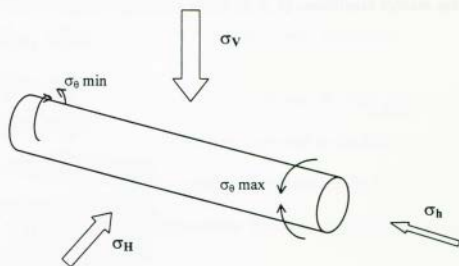


Fig. 2.16-Circumferential Stresses Around a Horizontal Wellbore⁴⁰

$$\sigma_r = \left(\frac{\sigma_x^0 + \sigma_y^0}{2} \right) \left(1 - \frac{R^2}{r^2} \right) + \left(\frac{\sigma_x^0 - \sigma_y^0}{2} \right) \left(1 + 3 \frac{R^4}{r^4} - 4 \frac{R^2}{r^2} \right) \cos 2\theta + \tau_{xy}^0 \left(1 + 3 \frac{R^4}{r^4} - 4 \frac{R^2}{r^2} \right) \sin 2\theta + P_w \frac{R^2}{r^2} \quad (2.53)$$

$$\sigma_\theta = \left(\frac{\sigma_x^0 + \sigma_y^0}{2} \right) \left(1 + \frac{R^2}{r^2} \right) - \left(\frac{\sigma_x^0 - \sigma_y^0}{2} \right) \left(1 + 3 \frac{R^4}{r^4} \right) \cos 2\theta - \tau_{xy}^0 \left(1 + 3 \frac{R^4}{r^4} \right) \sin 2\theta - P_w \frac{R^2}{r^2} \quad (2.54)$$

$$\sigma_z = \sigma_z^0 - \nu \left[2 \left(\sigma_x^0 - \sigma_y^0 \right) \frac{R^2}{r^2} \cos 2\theta + 4 \tau_{xy}^0 \frac{R^2}{r^2} \sin 2\theta \right] \quad (2.55)$$

$$\tau_{r\theta} = \left(\frac{\sigma_x^0 - \sigma_y^0}{2} \right) \left(1 - 3 \frac{R^4}{r^4} + 2 \frac{R^2}{r^2} \right) \sin 2\theta + \tau_{xy}^0 \left(1 - 3 \frac{R^4}{r^4} + 2 \frac{R^2}{r^2} \right) \cos 2\theta \quad (2.56)$$

$$\tau_{\theta z} = \left(-\tau_{xz}^0 \sin \theta + \tau_{xy}^0 \cos \theta \right) \left(1 + \frac{R^2}{r^2} \right) \quad (2.57)$$

$$\tau_{rz} = \left(\tau_{xz}^0 \cos \theta + \tau_{xy}^0 \sin \theta \right) \left(1 - \frac{R^2}{r^2} \right) \quad (2.58)$$

where the formation stresses expressed in the (x, y, z) coordinate system are:

$$\sigma_x^0 = l_{xx}^2 \sigma_H + l_{yy}^2 \sigma_h + l_{zz}^2 \sigma_v \quad (2.59)$$

$$\sigma_y^0 = l_{yx}^2 \sigma_H + l_{yy}^2 \sigma_h + l_{yz}^2 \sigma_v \quad (2.60)$$

$$\sigma_z^0 = l_{zx}^2 \sigma_H + l_{zy}^2 \sigma_h + l_{zz}^2 \sigma_v \quad (2.61)$$

$$\tau_{xy}^0 = l_{xx} l_{yx} \sigma_H + l_{xy} l_{yy} \sigma_h + l_{xz} l_{yz} \sigma_v \quad (2.62)$$

$$\tau_{yz}^0 = l_{yx} l_{xz} \sigma_H + l_{yy} l_{zy} \sigma_h + l_{yz} l_{zz} \sigma_v \quad (2.63)$$

$$\tau_{zx}^0 = l_{zx} l_{xx} \sigma_H + l_{zy} l_{xy} \sigma_h + l_{zz} l_{xz} \sigma_v \quad (2.64)$$

The superscript *o* on the stresses denote that these are the virgin formation stresses. And where l_{xx} , l_{xy} , l_{xz} are the direction cosines of the angles between the x-axis and the x' - y' , z' - axes, respectively.

l_{yx} , l_{yy} , l_{yz} are the direction cosines of the angles between the y-axis and the x' - y' , z' - axes, respectively.

l_{zx} , l_{zy} , l_{zz} are the direction cosines of the angles between the z-axis and the x' - y' , z' - axes, respectively.

The direction cosines relates to the angles *a* and *i* by:

$$l_{xx} = \cos a \cos i \quad (2.65)$$

$$l_{xy} = \sin a \cos i \quad (2.66)$$

$$l_{xz} = -\sin i \quad (2.67)$$

$$l_{yx} = -\sin a \quad (2.68)$$

$$l_{yy} = \cos a \quad (2.69)$$

$$l_{yz} = 0 \quad (2.70)$$

$$l_{zx} = \cos a \sin i \quad (2.71)$$

$$l_{zy'} = \sin a \sin i \quad (2.72)$$

$$l_{zz'} = \cos i \quad (2.73)$$

2.4 Mechanical Properties –Logs Correlations

Attempts to correlate mechanical properties to logs have been formulated elsewhere in the literature. In fact, it has been reported in the literature that relationships between porosity and mechanical properties of porous media do exist. Farquhar et al⁴¹ reported a simple exponential relationships between mechanical properties and the porosity, ϕ , of the general form:

$$M = A \exp^{B\phi} \quad (2.74)$$

where, M is some mechanical property and A and B are constants. Many researchers have used this relationship to describe their experimental data. The relationships are summarized in Table 2.1. Sarda, et al⁴² in their work on sand production based on the available data for various dry and saturated rocks found that for porosities up to 30% the unconfined compressive strength (σ_{ucs}) and the porosity (ϕ) are related as:

$$\sigma_{ucs} (MPa) = 258e^{-9\phi} \quad (2.75)$$

Table 2.1: Mechanical properties – Porosity correlation, $M = A \exp^{B\phi}$ constants⁴¹

Property (units)	Rock Type	Constants		Correlation coefficient
		A	B	
σ_{ucs} (Mpa)	Sandstone	208.08	0.074	0.71
	Carbonate	174.80	0.093	0.83
E_{STATIC} (GPa)	Sandstone	56.40	0.112	0.94
	Carbonate	69.05	0.060	0.87
$E_{DYNAMIC}$ (GPa)	Sandstone	55.39	0.146	0.96
	Carbonate	66.98	0.042	-

For the structure of Germigny-sous-Couloms for the 0-36% porosity interval, unconfined compressive strength (σ_{ucs}) and the porosity have the following curve fitting relationship:

$$\sigma_{ucs} (MPa) = 111.5e^{-11.6q} \quad (2.76)$$

Anderson et al⁴³ have presented an empirical relationship relating Poisson's ratio to shaliness for unconsolidated Gulf coast sands:

$$\nu = 0.125q + 0.27 \quad (2.77)$$

where q is the dispersed-shale index:

$$q = \frac{\phi_S - \phi_D}{\phi_S} \quad (2.78)$$

ϕ_S is computed using Wyllie et al equation (Tiab and Donaldson¹):

$$\phi_S = \left(\frac{\Delta t_{log} - \Delta t_{mat}}{\Delta t_{fl} - \Delta t_{mat}} \right) \frac{1}{B_{cp}} \quad (2.79)$$

B_{cp} compaction factor:

$$B_{cp} = \left(\frac{\Delta t_{sh}}{100} \right) B_{sh} \quad (2.80)$$

where 100 is the travel time for compacted shale in $\mu\text{sec}/\text{ft}$, and t_{sh} is the sonic travel time of adjacent shale. $B_{cp} = 1$ to 2 for sandstones.

The factor B_{sh} , is empirically determined, and is a function of clay type.

In shaly (clayey) unconsolidated formations the sonic porosity is calculated from the following equation:

$$\phi_S = \left(\frac{\Delta t_{log} - \Delta t_{mat}}{\Delta t_{fl} - \Delta t_{mat}} \right) \frac{1}{B_{cp}} - \left(\frac{\Delta t_{sh} - \Delta t_{mat}}{\Delta t_{fl} - \Delta t_{mat}} \right) V_{sh} \quad (2.81)$$

ϕ_D is the porosity obtained from density log computed as:

$$\phi_D = \left(\frac{\rho_{mat} - \rho_b}{\rho_{mat} - \rho_f} \right) \quad (2.82)$$

In shaly (clayey) formations:

$$\phi_D = \left(\frac{\rho_{mat} - \rho_h}{\rho_{mat} - \rho_f} \right) - \left(\frac{\rho_{mat} - \rho_{sh}}{\rho_{mat} - \rho_f} \right) V_{sh} \quad (2.83)$$

q has been defined differently by Tixier et al⁴⁴

$$q = \frac{\phi_{ig} - \phi_e}{\phi_{ig}} \quad (2.84)$$

where, ϕ_{ig} is the total space between the matrix grains supporting the overburden and,

ϕ_e is the porosity available to water and hydrocarbons.

2.4.1 In-Situ Stress Profiles

Cipolla et al⁴⁵ evaluated the use of log-derived stress profiles and measured stress profiles (in the Moxa Arch Frontier formation, southwestern Wyoming). The minimum horizontal stress is given as:

$$\sigma_{hmin} = \frac{\nu}{1-\nu} * (\sigma_v - P) + P + C \quad (2.85)$$

where:

σ_{hmin} = minimum horizontal stress, *psi/ft*,

σ_v = overburden stress = *1.0 psi/ft*,

C = correction constant = *0.133 psi/ft*, used to calibrate the log calculated stress to the measured stress,

P = pore pressure = 0.55 Psi/ft .

ν = Poisson's ratio

Equation 2.85 is derived from linear elasticity assuming oedometric deformation ($\epsilon_h = \epsilon_H = 0$).

Cipolla et al⁴⁵ found that the calculated stress in the shales compares favorably with the measured values. While the marine sand stress calculated using the *dipole sonic log* is somewhat low, compared to the measured value. Nevertheless, the general in-situ stress profile is reasonably predicted, using the calibrated *dipole sonic log*.

In the other hand, Cipolla et al⁴⁵ developed a correlation between in-situ stress and Gamma ray having the form:

$$\sigma_{h \min} = 0.105 \times V_{sh} + 0.745 \quad (2.86)$$

where: V_{sh} is the volume fraction of shale.

The comparison of the gamma ray-based stress profile and the measured stresses yielded good agreement.

Whitehead et al⁴⁶ obtained the following equation for the Travis Peak Formation of East Texas, between $\sigma_{h \min}$ and $\nu/(1-\nu)$, with a correlation coefficient of 0.924:

$$\sigma_{h \min} = 0.30342 \left(\frac{\nu}{1-\nu} \right) + 0.47399 \quad (2.87)$$

Also, Morales et al⁴⁷ presented the following correlation of the minimum horizontal stress:

$$\sigma_{h \min} = 0.4TVD + 0.58p_{res} \quad (2.88)$$

where

TVD = the true vertical depth, ft

p_{res} = the reservoir pressure, *psi*.

Eq. 2.88 was derived based on the equation

$$\sigma_{h \min} = \frac{\nu(0.95TVD - 2p_{res}) + p_{res}}{1 - \nu} \quad (2.89)$$

Setting Poisson's ratio, $\nu = 0.296$, value that minimizes the error between the predicted and measured closure stress values.

Woodland and J.S. Bell⁴⁸ showed that the interpreted closure stresses for 118 minifrac tests in Alberta have the following trends:

For depths less than 2300 m

$$\text{Closure stress} = 0.0114 Z + 3.1 \text{ Mpa}, R^2 = 0.56,$$

For depths greater than 2300 m

$$\text{Closure stress} = 0.0237 Z - 18.0 \text{ Mpa}, R^2 = 0.74,$$

For all depths

$$\text{Closure stress} = 0.0183 Z - 3.2 \text{ Mpa}, R^2 = 0.56,$$

Where Z = depth in meters.

Labudovic⁴⁹ stated, based on Eq.2.85 that the fracturing gradient is directly proportional to Poisson's ratio, and fractures would expand in height along the areas of low Poisson's ratio. Hence, the limits of upward or downward expansion of a created fracture would be in the areas of high Poisson's ratio.

Chapter 3

Hydraulic Fracturing in Hassi Messaoud

3.1 Reservoir Description

The Hassi Messaoud (HMD) structure lies approximately 800-km southeast of Algiers, Algeria (Fig. 3.1). It is a flattened, broad, oval anticline trending north-northeast to south-southwest, parallel to the major fault zone (Fig. 3.2). It covers almost 2,000 Km² in the Oued Mya basin. The first well, MD1 was drilled in 1956 and more than 1,000 wells have been drilled over the last 40 years. The field has been subdivided into 25 zones based on observed interwell pressure communication, the reservoir is in the Cambrian subdivided into four lithozones Ri, Ra, R2, and R3 (from the lower to the upper. Tables 3.1 and 3.2 show the average reservoir characteristics for HMD.

R3 lithozone:

Non-producing zone with a very low permeability and a high clay content averaging 30%(illite predominantly). The R3 section thickness increases from 275 m (902 ft) in well Md2 in the south central part of the field northward to 368 m (1207 ft) in well Omg57 north of the field.

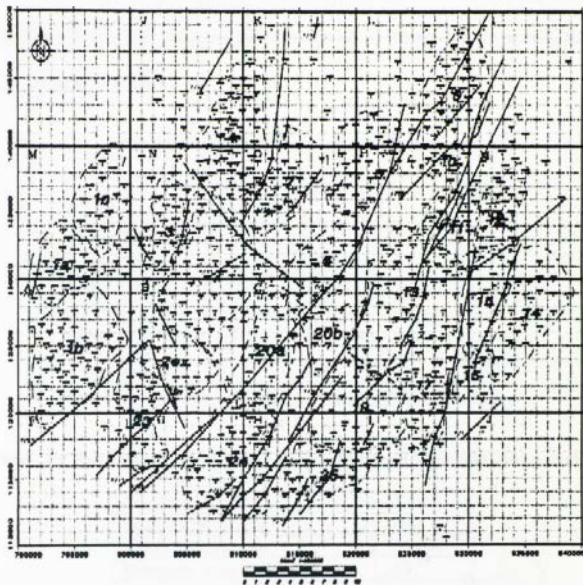


Fig. 3.2-Faults in Hassi Messaoud Structure

R2 lithozone:

It has a high clay content, averaging 20%, mainly illite with minor amount of kaolinite, occurring as interstitial clay and irregular thin interbeds of shale. R2 is a thick sequence of medium to coarse-grained sandstones. It has a good reservoir quality in the northern part of the field where water saturation is low. The R2 is considered the lower

boundary for the net interval due to the proximity to the water oil contact (WOC). R2 is subdivided into two layers: The upper R2 (R2-r1), and the lower R2 (R2-r2). R2-r1 has in general better reservoir characteristics than the latter. Where it is not eroded, R2 zone is about 80 m (262 ft) thick.

Table 3.1 Reservoir Properties by Lithozone

	Ri	Ra	R2	R3
K_{min} (md)	0.3	2	1	
K_{Ave} (md)	1	15	2.5	<1
K_{max} (md)	2	100	7	
ϕ_{min} (fraction)	0.06	0.06		
ϕ_{Ave} (fraction)	0.07	0.08	0.1	0.11
ϕ_{max} (fraction)	0.08	0.1		
$V_{th Ave}$ (%)	15	7	20	30
Swi(fraction)	0.17	0.10	0.17	0.17
H_{net}/H_{total}	0.5-0.9	0.8-1	0.65-0.8	0.65

Table. 3.2 Hassi Messaoud Average Characteristics (After McGowen et al⁵⁰)

Oil gravity ° API	43.5-45
Initial GOR scf/bbl	1000
Water Salinity ppm	360,000
Reservoir Temperature °F	245
Average Porosity %	7.5
Average Permeability to oil md	1-50
Initial oil saturation %	80-95
Gross formation Thickness ft	200-500
Net formation Thickness ft	100-300

Ra (anisometric zone):

The Ra zone has a maximum total thickness of 150 m (492 ft) in the western portion of the field, it is considered the primary reservoir. The Ra zone is fine-grained quartzite sandstone. Ra zone has been subdivided into five subzones highly laminated

with silts and black shale, that are, from the upper to the lower: D4, D3, D2, ID, and D1. The predominant clay mineral in Ra is kaolinite. D5, D4, and D3 drains are eroded in the central northern portions of the field.

Ri (isometric zone):

Also referred to as D5, is a 50 m (164 ft) thick quartzitic sandstone unit, it is characterized as a uniformly thick, well sorted, medium grained sandstone with interbeds of shale and siltstone. D5 is not considered as a significant producing zone because of its poor reservoir characteristics. The predominant clay mineral in layer D5 is illite.

3.2 Hydraulic Fracturing in HASSI MESSAOUD

Early hydraulic fracturing treatments were performed in HMD and the surrounding fields, approximately 20 operations during the 1970's and the 1980's McGowen et al⁵⁰, and even earlier in the 1960's. Most of the treatments were performed on low productivity wells and were designed with for large fluid and proppant volumes, similar to the massive hydraulic fracturing being performed in the United States. Nevertheless, production results were very poor with only a couple of wells responding favorably. In addition, high treating pressures and unexplained screen outs complicated many treatments. A failure caused by an early screen out while fracturing GS13, a well in the nearby EL GASSI field, in 1983 resulted in ending the hydraulic fracturing experience in Algeria, until 1990⁵⁰.

3.2.1 Discussion of the Results of Hydraulic Fracturing in HMD

One has to point out that the obtained results, that will be discussed later, are mainly governed by in situ stress field. The operating conditions such as sand plugs and perforating. In HMD, sand plugs of 40/70 or 20/40 Ottawa sands are placed, based on well data such as oil and water saturation profiles, stress profile determined using the previously described stress correlation, via coiled tubing to obtain stress barriers to prevent downward fracture propagation to low stress, high water, undesirable zones. These sand plugs have allowed fracture propagation without significant growth into underlying undesirable zones⁵⁰. Also, perforations are performed by shooting 3-6 shots/ft over a minimum of 20-40 feet, in slotted liner and cemented liner completions. In new completions, perforation location is chosen depending on the desired fracture initiation point, while in slotted liner completions it is chosen based on the stress profile and normally covers the region of the lowest stress⁵⁰. Nevertheless, the existence of perforations has little effect (if any) influence on the orientation of hydraulically induced fractures⁵¹. Generally hydraulic fractures initiate on the borehole wall perpendicular to the least principal stress. The analysis of the available data of fracturing in Hassi Messaoud field shows that the created fractures seem to have a preference for the layers ID, D1, and D4 (Figures 3.3, 3.4). Layer D4 is not observed, in several regions of the field. The reason may be due to the fact that D4 was eroded (east and south east of the structure, zones: 14, 15, 16, 17, 19 and northeast zone 25). It may also be due to the fact that D4 was eroded, with D5 and sometimes with D3 and D2, in the central northern portion of the field (east of zone 3, zones 6, 7, and 9).

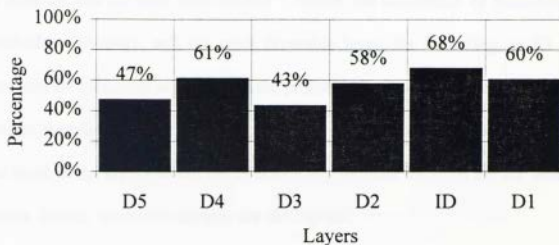


Fig. 3.3-Overall Frequency of Fracturing by Layer in HMD

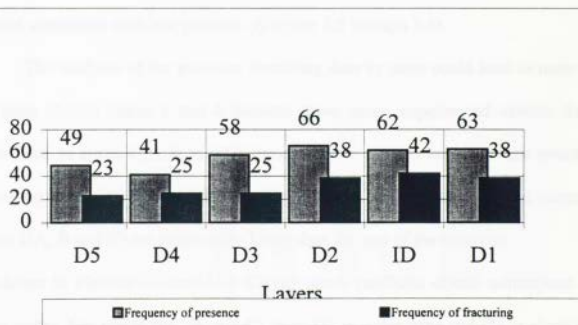


Fig. 3.4-Overall Presence of Layers and Frequency of Fracturing

In zones 8 and 13 the erosion was so severe that it reached even the ID. In the eastern part of zone 2N, southeast zone 2E, zone 4, northern part of zone 20A and zone 20B both D4 and D5 have been eroded⁵². Hence, the occurrence of fracturing seems to be linked to lithology, and the most favorable layer, for fracturing, is ID layer. The layers may be classified according to the probability of occurrence of induced hydraulic fractures decreasingly: ID, D4, D1, D2, D5 and D3. Layers D3 and D5 could be considered as the layers where the hydraulically induced fractures are the more unlikely to occur. Hence, where the stresses are the highest.

Back analyzing the composition of these layers could lead to a tangible explanation. Indeed, the analysis of the sedimentology of four zones situated in the southern side of the structure⁵³ (zones: 1B, 17, 19, and 25) shows that, comparing to the other layers of Ra zone, layers D5 and D3 have the particularity of having a high clay content associated with low porosity. (Figures 3.5 through 3.8).

The analysis of the previous fracturing data by zone could lead to more details. We have chosen zones 1 and 2 because these zones experienced several fracturing operations. In zones 1(A, B, and C) situated in the western section of the structure, the producing layers are D5 and D4 the lower layers, D2, ID and D1, are water zones. Zones 1(A, B and C) are structurally lower than the rest of the reservoir. As shown in Figures 3.9 and 3.10 Clayey zones (stiffness effect) correspond to high stress zones. For zones 1(A, B, and C) layer D2 is water zone and D3 is close to water zone. For zones 2 (N, S, and EX) the potential layers for fracturing are ID and D2 then layers D5 and D4. D3 is likely to be a layer where stress concentration exists for the same reasons explained above, as shown in Figures 3.11 and 3.12.

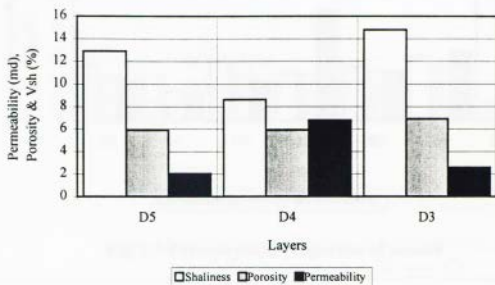


Fig. 3.5-Petrophysical Properties of Zone 1B

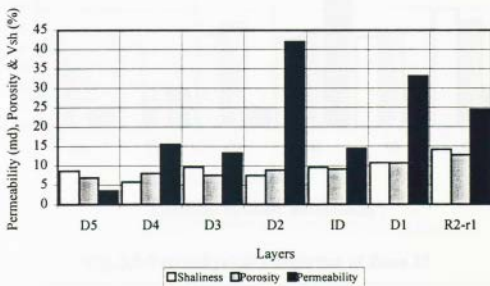


Fig. 3.6-Petrophysical Properties of Zone17

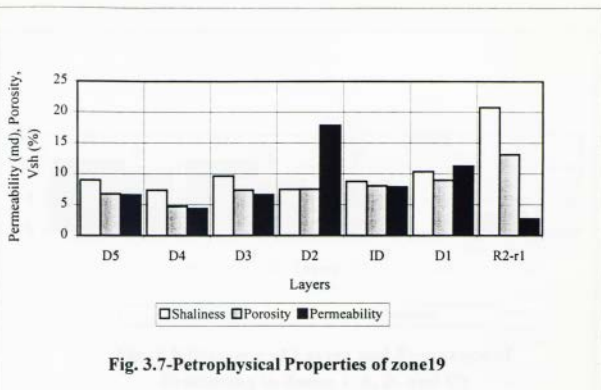


Fig. 3.7-Petrophysical Properties of zone19

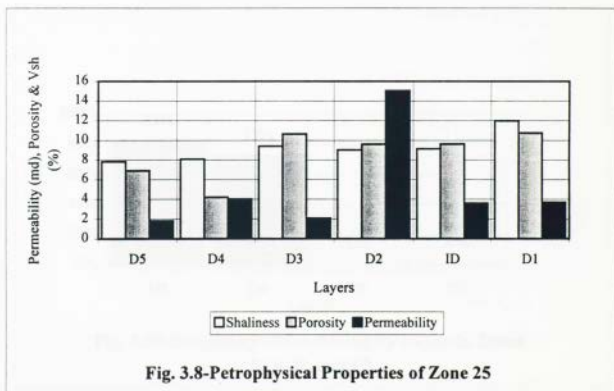


Fig. 3.8-Petrophysical Properties of Zone 25

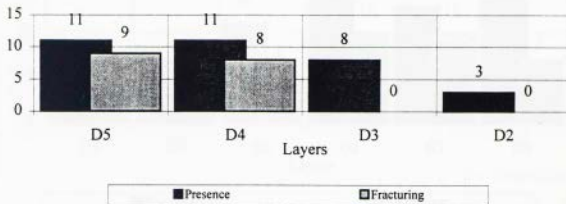


Fig. 3.9-Presence of Layers and Frequency of Fracturing in Zones 1(A, B, and C)

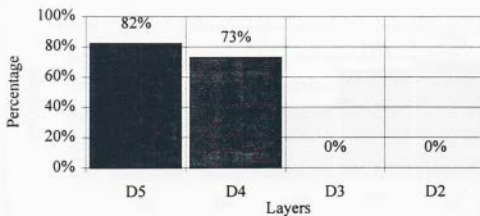


Fig. 3.10-Frequency of Fracturing by Layer in Zones 1 (A, B, and C)

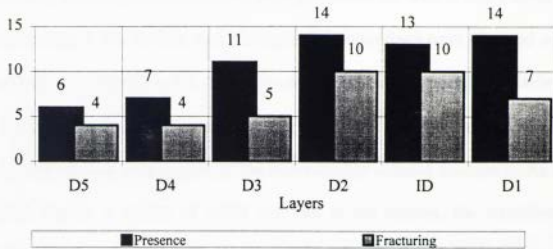


Fig. 3.11-Presence and Fracturing of Layers in Zone 2 (N, S, and EX)

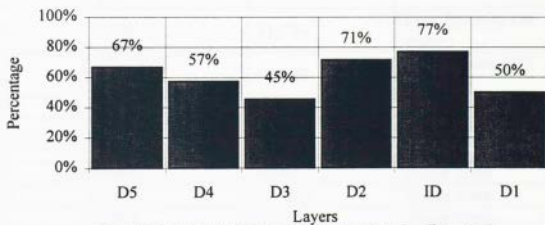


Fig. 3.12-Frequency of Fracturing by Layer in Zones 2 (N, S, and Ex)

3.2.2 Microfrac Measurements in HMD Field

In 1992, microfrac measurements were performed on Well A and a stress profile was obtained (Fig. 3.13). In fact, seven interpretable microfracs were obtained over 160 m of open hole from Ra-D2 to R3. The observed results are summarized in Table 3.3. Hence, the layer Ra-D1 is contained between two zones of high stresses constituting barriers for the vertical propagation of the hydraulically induced fracture in Ra-D1. At the Top the Ra-ID, a barrier of 3,650 psi, and at the bottom, the transition zone, constituting a barrier of 750 psi. Further down, the R2-r2 is a more important barrier of 3,100 psi will hinder any downward propagation of a hydraulically induced fracture in the Ra-D1 layer.

Table 3.3 Microfracturing Measurements of Well A Results

Layer	Location of the minimum of $\sigma_{h \min}$ (m)	Minimum Stress (psi)	Observation
Ra-D2	3402	11,750	Low Porosity Oil zone
Ra-ID	3420	12,100	Low Porosity Oil zone
Ra-D1	3442	8,450	Oil zone
Sandy Mound	3460	9,200	Top of the transition zone
R2-r1	3480	9,600	Water zone
R2-r2	3521	11,550	Water zone
R3	3562	10,150	Water zone

These results obtained, Belhaouas et al⁶ tried to correlate the stress profile with logs. The first step was to correlate the acoustic Young's modulus with logs, from 1,727 samples in well A from a sedimentary sequence of 263 m crossing the Cambrian from

the top of Ri to 30 m in R3. The result was a correlation, linking dynamic Young's modulus to porosity and shaliness, with a coefficient of correlation of 0.96.

$$E = 12.62 - 0.4318\phi_e - 0.0994V_{sh} \quad (3.1)$$

where,

E = dynamic Young's modulus expressed in $10^6 psi$,

ϕ_e = the effective porosity expressed in %, and

V_{sh} = the shale content expressed in %.

The second step correlates the minimum horizontal stress with logs. A relationship between minimum horizontal stress, Young's modulus, and oil saturation was obtained with a coefficient of correlation of 0.98.

$$\sigma_{hmin} = 6,163.1 + 1312.2E - 74.416S_o \quad (3.2)$$

where,

σ_{hmin} = the in situ stress expressed in psi ,

E = Young's modulus expressed in $10^6 psi$,

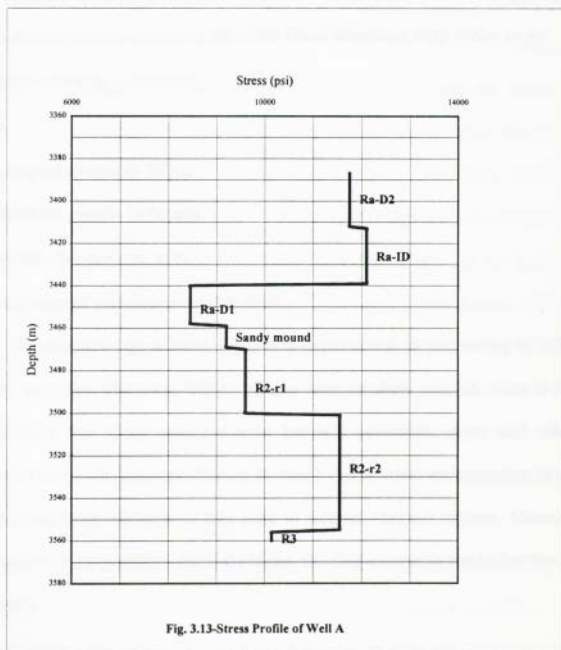
S_o = the oil saturation expressed in %.

And since this correlation has been used to predict the stress profile from open hole logs, for design purposes, throughout Hassi Messaoud field and even in near by fields (EL GASSI, EL AGREB, ZOTTI).

3.2.3 Discussion of The Correlations

3.2.3.1 Young's Modulus – Logs Correlation

Equation 3.1 was obtained for over than 1,700 samples, with a coefficient of correlation of 0.96. Similar correlations were obtained for two other wells, Well B, situated 11 Km east of A:



$$E = 12.83 - 0.5271\phi_e - 0.1388V_{sh} \quad (3.3)$$

Where:

E = Young's modulus in $10^6 psi$,

V_{sh} = the shale content in %, and

ϕ_e = the effective porosity in %.

The coefficient of correlation equal to 0.87.

Well C, situated on the southern side of the Hassi Messaoud field 30Km away:

$$E = 12.21 - 0.4040\phi_e - 0.0842V_{sh} \quad (3.4)$$

where:

E = Young's modulus in $10^6 psi$,

V_{sh} = the shale content in %, and

ϕ_e = the effective porosity in %.

The coefficient of correlation equal to 0.90.

The negative sign in front of porosity term reflects the decreasing of stiffness as porosity increases. However, this is not the case for shale content, since it has been demonstrated that stress contrasts exist between permeable zones and other non-permeable zones, the latter constituting barriers^{28, 34}. The stress concentration in a zone is associated with the stiffness of this zone in tectonic stressed regions. Moreover it is associated with clay content, since the higher the clay content is, the higher the stiffness of a rock.

3.2.3.2 Minimum Horizontal Stress – Logs Correlation

Correlating the minimum horizontal stress to log derived properties could be an interesting approach. However, the obtained relationship (Eq. 3.2) presents some confusion. In fact, the obtained stress profile presents an extreme fluctuation due to the variations in the hydrocarbon saturation profile. Also, water zones underlying the oil zones are considered stress barriers, however field observations of hydraulic fracturing results throughout the HMD field show that water zones could be fractured with relatively low closure pressures. Young's modulus term reflects the tectonic aspect influencing the stress. The positive sign reflects the fact that the higher the stiffness of a horizon, the higher the horizontal stress values. Hence, the likely term to cause fluctuations is the oil saturation term. It would be more representative if the term pore pressure were introduced rather than oil saturation to account for the pore pressure effect on total stress (concept of effective and total stress). Nevertheless, pore pressure will not severely affect the stress contrast between different layers. Hence, it could be neglected. Moreover, fracturing occurrence in Hassi Messaoud seems to be lithology dependent, high stress values are found to be associated with high shaliness values as well as low porosities. For future correlation attempts, average parameters by layer must be considered.

The stress profile of well A (Fig. 3.14) shows that there is no correlation of minimum horizontal stress involving depth as a unique correlating parameter.

The first attempts were conducted toward correlating the minimum horizontal stress and $\frac{\nu}{1-\nu}$, based on the results of microfracturing tests obtained in well A, as well

as in two other wells, where the created fracture was confined in a unique layer, and where compressional and shear transit time logs are available as well. These attempts were unsuccessful, showing that care is to be taken when dealing with the relationship:

$$\sigma_{hmin} = \frac{\nu}{1-\nu} \sigma_v \quad (3.5)$$

where: σ_{hmin} = the minimum horizontal stress, *psi*,

σ_v = the Vertical principal stress, in *psi*, and

ν = Poisson's ratio.

Similar unsatisfactory results were obtained when trying to correlate the in-situ stress and gamma ray response as well as Young's modulus E, and Poisson's ratio, ν . However, based on the observations obtained from the analysis of fracture treatment, a good fit was obtained between the stress data of well A in addition to stress values obtained from wells Om1602 and MD99. Because that in these two wells the created fractures seem to be some how created in a single layer with little incursion into adjacent layers, correlating σ_{hmin} with the shaliness V_{sh} and the porosity ϕ , yields the following (with R^2 equal to 0.89)

$$\sigma_{hmin} = 58.88 \times V_{sh} - 508.82 \times \phi + 12,627 \quad (3.6)$$

This correlation leads to an average deviation between the measured and the calculated stresses of only 8.46% (Table 3.4 and Fig. 3.15).

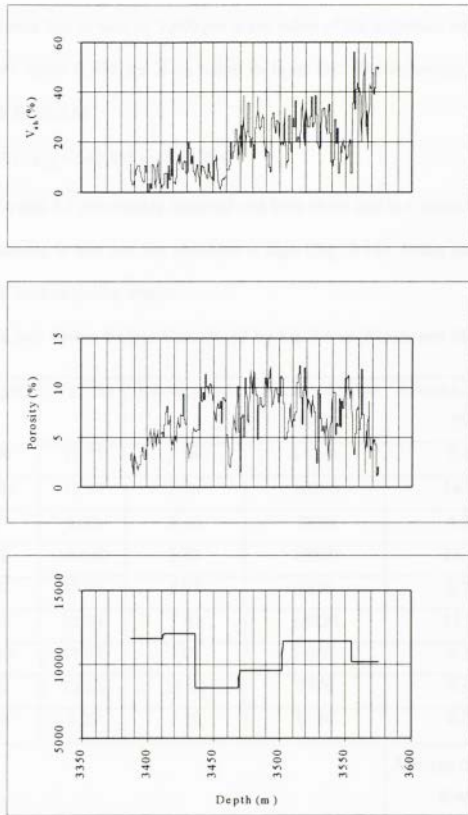


Fig. 3.14-Stress, Shaliness, and Porosity Profiles of well A

In well A, the stress value obtained for the Sandy Mound is roughly equal to the value obtained for R2-r1. Based on this fact and the thickness of the sandy mound is low, it is believed that in well A, 9,600 *psi* is the value of the minimum horizontal stress in layer R2-r1 while 8,450 *psi* is its value in layer D1. The following equation was obtained with R² of 0.88.

$$\sigma_{h\min} = 56.561 \times V_{sh} - 642.358 \times \phi + 13,886 \quad (3.7)$$

Equations. 3.6 and 3.7 are roughly identical and both show that is a stress barrier a layer where the porosity is low and the shaliness is high (Fig. 3.14). Using either Eq.3.7 or Eq. 3.6 would lead to similar results.

Table 3.4: Stress Values Calculated by Eq. 3.6 vs. Measured Stresses

Stress (<i>psi</i>)	V _{sh} (%)	Porosity (%)	Calculated stress (<i>psi</i>)	Average deviation (%)
11750	11.73	3.89	11340	3.49
12100	11.57	5.74	10390	14.15
8450	8.52	8.44	8830	4.53
9200	14.640	5.03	10930	18.79
9600	23.97	8.87	9530	0.76
11550	25.06	7.63	10220	11.51
10150	32.98	7.02	11990	8.32
7730	12.83	11.02	7770	0.58
8670	4.29	7.32	9150	8.72
				Average deviation: 8.46%

Figure. 3.16 shows the variation of the fracturing gradient throughout HMD structure. It appears that the fracturing gradient tends to increase as we move from the

eastern portion of the reservoir to the western side. Indeed, fracturing gradient takes its lowest values in the northeast side (zone 9). As we move southward towards zones 13, 13S and towards zone 15, the fracturing gradient experiences a slight increase, reaching an average value of 0.84 *psi/ft* in south zone 19, the western portion of zone 24 and zone 25. As we go westward through zone 19, zone 20 A, B, zone 24, zone 23, zones 2N, S and Ex and zone 3 the fracturing gradient goes up. It reaches its highest values in zone 1 at the west of the reservoir, averaging 0.95 *psi/ft*.

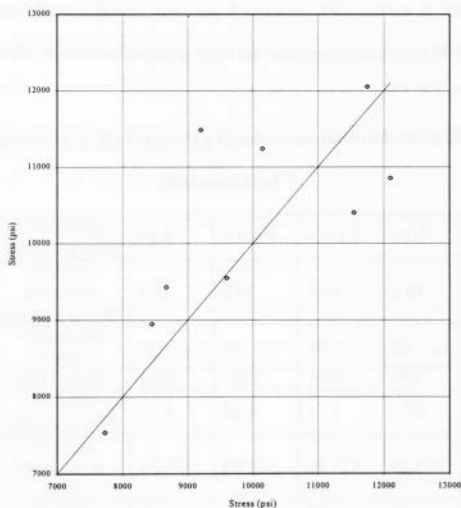


Fig. 3.15-Measured vs. Calculated Stresses

In summary, the eastern part of HMD structure has relatively low fracturing gradients, which starts to increase as we move westward. It reaches its highest values in zone 1. This map fits the structural geology of HMD reservoir (Fig. 3.2) and it confirms the fact that the structure is split into two principle compartments the western and the eastern by the major fault NE-SW ONI17 to MD395. Also this statement may be of considerable importance, considering that production gain is severely reduced as the fracturing gradient increases⁵⁰ as shown in Tables 3.5 and 3.6. The reason they stated for that is the increased occurrence of non-Tip screen outs leading to drastic reduction of the proppant amount placed into the formation. This makes it risky to select candidate wells for hydraulic fracturing from the western compartment of the structure.

Table 3.5 Influence of the Fracturing Gradient on the Production Gain (After McGowen et al⁵⁰)

Fracturing gradient (<i>psi/ft</i>)	<0.8	0.8-0.9	0.9-1.0	>1.0
Average fracturing gradient (<i>psi/ft</i>)	0.72	0.85	0.94	1.04
Number of wells	19	38	28	13
KH (md-ft)	2321	1415	1484	982
Average efficiency (%)	11.0	16.5	17.5	17.0
Average Proppant in (lbs)	75,343	89,360	85,777	62,695
% TSO	42	34	36	31
% Non-TSO	11	5	18	23
Average gain (bopd)	1327	562	554	408

Table 3.6 Screen out Occurrence in HMD (After McGowen et al⁵⁰)

Screen out type	None	TSO	Non-TSO
Number of wells	51	35	12
Average KH (md-ft)	1182	2055	1662
Average fluid efficiency (%)	16.9	13.1	18.9
Average fracturing gradient (psi/ft)	0.87	0.87	0.92
Average Proppant in (lbs)	101946	70423	31662
Average gain	720	878	-4

3.3 In-Situ Stress Orientation in HMD

Using Eqs. 2.54, 2.59, 2.60, 2.62, in addition to Eqs. 2.65 through 2.70 horizontal borehole maximum and minimum circumferential stresses corresponding respectively to an angle θ of $\pi/2$ or $3\pi/2$ and 0 or π , are calculated and presented in Figures 3.17 and 3.18, as well as in Table 3.7.

If we consider a state of stress where $\sigma_v > \sigma_H > \sigma_h$, the well azimuth where borehole stability issues are the more unlikely to occur corresponds to a direction parallel to the minimum horizontal stress. Figures 3.17, and 3.18 show the predicted effect of well trajectory on wellbore stability for different principal stress values. The most stable direction is the one parallel to minimum horizontal stress.

Early breakthrough, due to the proximity of injection wells from a hydraulically fractured well, could be controlled by appropriate design of the fracture dimensions or by avoiding considering wells, situated close to injection wells, as potential candidates for hydraulic fracturing.

In Hassi Messaoud, UBI (Ultrasonic Borehole Imager) has been used to analyze the stress induced borehole breakouts on 15 wells corresponding to⁵⁵:

- 3 wells in zone 9, situated in the northeastern part of the structure,
- 3 wells in zones 20A and 20B situated in the central portion of the structure,
- 2 wells in zone 15, situated in the eastern flank of the structure,
- 2 wells in zone 24, 1 in zone 25 and 1 in zone 17, all situated in the southern side,
- 2 wells in zone 2 and 1 in zone 3 situated in the western flank of the formation.

Despite the existence of caves in addition to the proximity of faults of some wells the predominant direction of the breakouts is NE-SW corresponding to a general orientation of the maximum stress being SE-NW.

MASSA et al⁵⁶ studied fracturing of Hassi Messaoud using cores oriented by the dipping of the layers. It is to be mentioned that at that time other methods were, unsuccessfully used, such as the orientation of cores by natural remnant magnetization, oriented coring, and use of borehole televiewer. This study made it evident that the orientation of the faults is mainly 45-50° azimuth. Hence, the orientation of the maximum Horizontal stress obtained using the UBI is perpendicular to the general trend of faults in HMD. Also, it is consistent with the orientation of HMD anticline. The Hassi Messaoud anticline orientation is therefore, the result of compressive maximum horizontal stress acting in the SE-NW direction. Moreover, this orientation matches the results obtained by both: Beghoul's study³ of breakouts in Timimoun basin and Tiab's study⁴ of the natural fractures orientation in Ahnet basin.

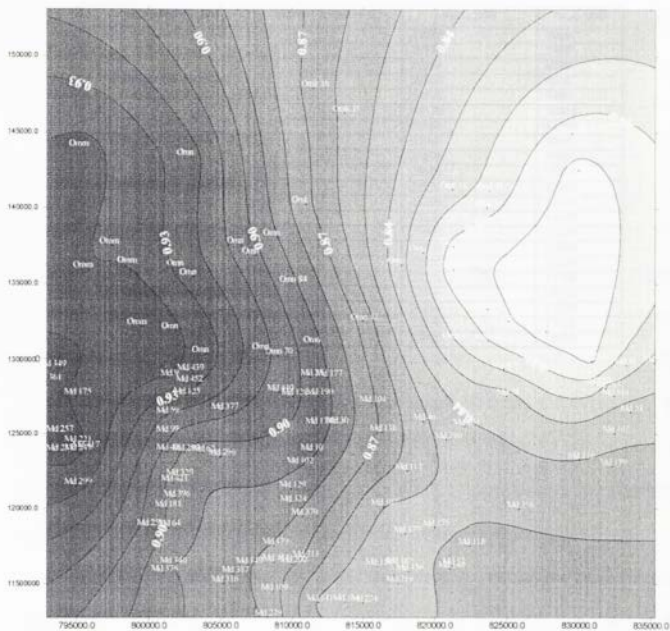


Fig. 3.16-Isofracturing Gradient Map of Hassi Messaoud Structure

Table 3.7 Circumferential Stresses Around a Horizontal Borehole

σ_v , σ_H , and σ_h (psi)	Azimuth angle α ($^\circ$)	$\sigma_{\theta \max}$ (psi)	$\sigma_{\theta \min}$ (psi)
10000, 8000, and 6000	0	21000	5000
	15	20870	5400
	30	20500	6500
	45	20000	8000
	60	19500	9500
	75	19130	10600
	90	19000	11000
	12000, 10000, and 8000	0	25000
15		24870	9400
30		24500	10500
45		24000	12000
60		23500	13500
75		23130	14600
90		23000	15000
12000, 11000, and 10000		0	23000
	15	22930	15200
	30	22750	15750
	45	22500	16500
	60	22250	17250
	75	22070	17800
	90	22000	18000

Chapter 4

Discussion of Stress Correlation Application in Hassi Messaoud

4.1 Application of the New Correlation

Figures 4.1 through 4.6 show that the correlation (Eq. 3.6) predicts the zone where the in-situ stress is lowest, allowing the initiation and the propagation of a fracture. In wells Oml602 (Fig. 4.1), Omn402 (Fig. 4.2), MD440 (Fig. 4.3), MD452 (Fig. 4.4). Though, the pressure response of well Oml852 (Fig. 4.5) was not interpreted because of the fact that communication existed between the tubing and the casing, The stress profile predicts the location of the created fracture, from the perforated layer D2 with a value of minimum horizontal stress of 9,700 psi, to layer ID with a value of $\sigma_{h,min}$ of 9,400 psi. For MD99 (Fig. 4.6), the predicted in situ stress for the perforated interval is 9,500 while in-situ stress obtained from pressure decline data is 8,670 psi.

In some cases, even though the stress profile predicts the location of the created fracture, it overestimates the value of the in-situ stress. For well Omn541 (Fig. 4.7) the layers that are likely to be fractured are D2 to the bottom, which is the case. However, the in situ stress predicted is between 9,100 and 10,000 psi, which that are different from the measured 7,800 psi.

The stress profile can underestimate the stress value. In fact, for well Omn70 (Fig. 4.8) it predicts a fracture initiating in D2 layer where the in-situ stress is 7,140 psi, and the treatment revealed a fracture in both ID and D2. Hence, the created fracture could have probably been initiated in D2 than it migrated toward ID, if the treatment

were not stopped D1 and R2 were to be fractured, the reel value of $\sigma_{h, \min}$ was 9,200 psi. In well Omn84 (Fig. 4.9) the stress profile predicts that all layers would be fractured, which was the case. Nevertheless, it underestimates the stress value, which is, in reality, equal to 9,430 psi.

Equation 3.6 seems to be not only applicable for Hassi Messaoud reservoir but also for the near by El GASSI and El AGREB reservoirs situated respectively at 100 and 140 Km Southwest HMD. Indeed, for well GS7 (Fig. 4.10) the in-situ stress value predicted for layer D4 is roughly equal to the measured value (8,700 *psi*). For well AR22 (Fig. 4.11) the stress profile predicts a fracture in D3 layer with a closure stress of 8,090 psi the real in situ stress value was 7,600 psi. However, the temperature profile shows that part of layer D4 was fractured. According to the stress profile this could be due to the incursion of the fracture into the lower part of D4 that the stress level is 8,700 psi. In well GS14, (Fig. 4.12) both predicted and reel stress values and fracture location match perfectly. The stress profile predicts a creation of a fracture contained in between layers D4 and ID that are a kind of stress barriers, D3 and D2 being layers were In situ stresses are low equal to 6,700 psi. Surprisingly, this is the exact value obtained from the interpretation of the fall off data. Also, the temperature profile shows a cool portion corresponding to layers D3 and D2. Table. 4.1 is a summary of the application of the obtained correlation.

Table 4.1 Summary of the Results of the Application of the Obtained Correlation

Well	Location	Predicted interval to be fractured	Fractured interval	Predicted P_{ef} (psi)	Reel P_{ef} (psi)	Observation
Oml602	HMD	R2	R2	7500	7730	Good predictions
Omn402	HMD	D2 and ID	D2 and ID	9600	8800	Good predictions
MD440	HMD	D2 to D1	D2 to D1	8200-9100	8800	Good predictions
MD452	HMD	ID bottom to	all layers	8200-11300	10900	The fracture was created up then it migrated downward
Oml852	HMD	D2 and ID	D2 and ID	9700-9400	-	Good predictions
MD99	HMD	D4 to D2	D4	9500	8670	D4 was perforated and was taking fluid
Omn541	HMD	D2 to bottom	D2 to bottom	9000-10000	7800	The stress correlation overestimates the stress value
Omn70	HMD	D2 and ID	D2 and ID	7200-8400	9200	The stress correlation underestimates the stress value
Omn84	HMD	all layers	all layers	6500-9000	9430	The stress correlation underestimates the stress value
GS7	EL GASSI	D4	D4	8200	8700	Good predictions
Ar22	EL AGREB	D4 and D3	D4 and D3	8100-8700	7600	Good predictions
GS14	EL GASSI	D3	D4 and D3	6700	6700	Good predictions

4.2 Comparison Between HMD Correlation and the New

One

The correlations used in Hassi Messaoud are as follows

$$E = 12.62 - 0.4318\phi_e - 0.0994V_{sh} \quad (3.1)$$

$$\sigma_{h\min} = 6,163.1 + 1312.2E - 74.416S_o \quad (3.2)$$

In fact the minimum stress correlation used in HMD is a correlation of minimum horizontal stress with porosity, shaliness, and oil saturation. The combination of Eqs. 3.1 and 3.2 is given as

$$\sigma_{h\min} = 22,723.06 - 566.6\phi_e - 130.43V_{sh} - 74.416S_o \quad (4.1)$$

Comparing Eq. 4.1 and Eq. 3.6 it is evident that in both equations the effect of ϕ_e is more important than the effect of V_{sh} . In Eq. 4.1 the multiplying factor of ϕ_e is 4 times the multiplying factor of V_{sh} . While in Eq. 3.6 the multiplying factor of ϕ_e is 8 times the multiplying factor of V_{sh} , though in the former equation V_{sh} has a negative sign. In general, in both correlations minimum horizontal stress is a function of porosity and shale volume. This could be taken as the validation of the obtained correlation knowing that, in practice, the stress correlation used in HMD was observed to predict the fracture location, however its predicted values of minimum horizontal stress are generally different from the real values.

Belhaouas et al⁶ reported that in their study of tens of wells fractured using the Hassi Messaoud stress profile correlation, fracture locations have been successfully predicted, these wells included: case of MD53, MD311, MD329, MD369, and Omn342.

In well Omn402 (Fig. 4.13) the temperature log following the treatment shows a fracture in layers D2 and ID which is the interval predicted by HMD minimum horizontal stress correlation profile. However, the predicted value of minimum stress (11,000 psi) overestimates the real value. For the case of well MD452, Fig. 4.14, the created hydraulic fracture extends from D3 to R2. Hence, not only has HMD stress profile overestimated the stress value but also it revealed a stress barrier, of 13,000 psi, stretching from top of D3 to 3400 m. This means the fracture would have to break to get the real fracture height. Similarly, HMD stress profile succeeded in predicting the location of the hydraulic fracture in well Om1852, nevertheless it is impossible to check whether or not it predicted the right stress value (Fig. 4. 15). Also, HMD stress profile can predict the fracture location in the case of wells Omn541, and Omn70, but it overestimates the stress value (Figs. 4.16, and 4.17). HMD stress profile fails to predict neither the value of the minimum horizontal stress nor the location of the hydraulic fracture in the case of wells MD440, MD99, and Omn84. (Figures 4.18 through 4.19).

4.3 Sensitivity Analysis of the Correlation

Figures 4.20, 4.21 and Tables 4.2, 4.3 show how important is the effect on stress of the porosity of the rock. Also, the correlation leads to acceptable values of stress for porosity values in-between 5 and 15%, which is the case for Hassi Messaoud reservoir, thus, it cannot be extrapolated. However, the effect of shaliness is lower, the stress slope is less steep, and the predicted stress values are quite reasonable for a wide range of V_{sh} .

Table 4.2: Stress Sensitivity to Vsh

ϕ %	Vsh%	$\sigma_{h \text{ min}}(\text{psi})$	ϕ %	Vsh%	$\sigma_{h \text{ min}}(\text{psi})$	ϕ %	Vsh%	$\sigma_{h \text{ min}}(\text{psi})$
5	0	10674	10	0	7462	15	0	4251
5	5	10957	10	5	7745	15	5	4533
5	10	11240	10	10	8028	15	10	4816
5	15	11523	10	15	8311	15	15	5099
5	20	11805	10	20	8594	15	20	5382
5	25	12088	10	25	8876	15	25	5665
5	30	12371	10	30	9159	15	30	5947
5	35	12654	10	35	9442	15	35	6230
5	40	12937	10	40	9725	15	40	6513
5	45	13219	10	45	10008	15	45	6796
5	50	13502	10	50	10290	15	50	7079
5	55	13785	10	55	10573	15	55	7361
5	60	14068	10	60	10856	15	60	7644

Table 4.3: Stress Sensitivity to ϕ

ϕ %	Vsh%	$\sigma_{h \text{ min}}(\text{psi})$	ϕ %	Vsh%	$\sigma_{h \text{ min}}(\text{psi})$	ϕ %	Vsh%	$\sigma_{h \text{ min}}(\text{psi})$
2	5	12884	2	10	13167	2	20	13733
3	5	12242	3	10	12525	3	20	13090
4	5	11599	4	10	11882	4	20	12448
5	5	10957	5	10	11240	5	20	11805
6	5	10315	6	10	10597	6	20	11163
7	5	9672	7	10	9955	7	20	10521
8	5	9030	8	10	9313	8	20	9878
9	5	8388	9	10	8670	9	20	9236
10	5	7745	10	10	8028	10	20	8594
11	5	7103	11	10	7386	11	20	7951
12	5	6461	12	10	6743	12	20	7309
13	5	5818	13	10	6101	13	20	6667
14	5	5176	14	10	5459	14	20	6024
15	5	4533	15	10	4816	15	20	5382
2	30	14298	2	40	14864	2	50	15429
3	30	13656	3	40	14221	3	50	14787
4	30	13013	4	40	13579	4	50	14145
5	30	12371	5	40	12937	5	50	13502
6	30	11729	6	40	12294	6	50	12860
7	30	11086	7	40	11652	7	50	12218
8	30	10444	8	40	11010	8	50	11575
9	30	9802	9	40	10367	9	50	10933
10	30	9159	10	40	9725	10	50	10290
11	30	8517	11	40	9083	11	50	9648
12	30	7875	12	40	8440	12	50	9006
13	30	7232	13	40	7798	13	50	8363
14	30	6590	14	40	7155	14	50	7721
15	30	5947	15	40	6513	15	50	7079

Hence, the obtained correlation leads to acceptable results as long as porosity is <15%, and for a wide range of V_{sh} ; in HMD, this correlation would therefore give reasonable stress values.

4.4 General Considerations

The in-situ stress profile could be used to predict fracture containment. In general, in HASSI MESSAOUD, layer D5, the upper layer bounding the main producing reservoir Ra, is a layer where the porosity is very low and the shaliness is high, making it a potential barrier. However, for the lower bounding layers though the shaliness increases the porosity, which impact on stress concentration seems to be the higher (Eqs. 3.6 and 3.7), increases leading to a decrease in the stress value as we go deeper in the reservoir. Hence, in the bottom layers, the low stress level is low makes them favorable for a downward propagation of a created fracture.

The risk of having tubing or packer failure is high in wells where the fracturing gradient is high. Working tubing pressure is limited to 9,000-10,000 psi while bottomhole-fracturing pressures often exceed 11,000 psi, and it happens that tubing failure occurs especially at screen outs. Packer failure occurred on about 5% of all the treatment attempts⁵⁰. Failures have been almost exclusively in the larger tubing sizes which, in the case of wells being treated, are often used the more (4 ½" and 5" tubing sizes, together, represent 65% of the cases).

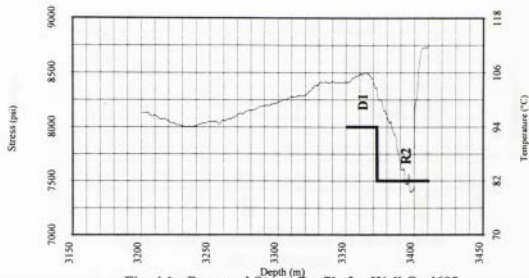


Fig. 4.1 - Proposed Stress Profile for Well Om1602
(Pcl = 7730 psi)

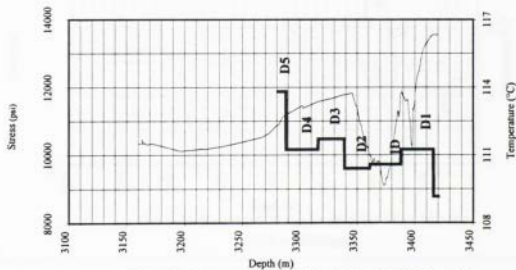
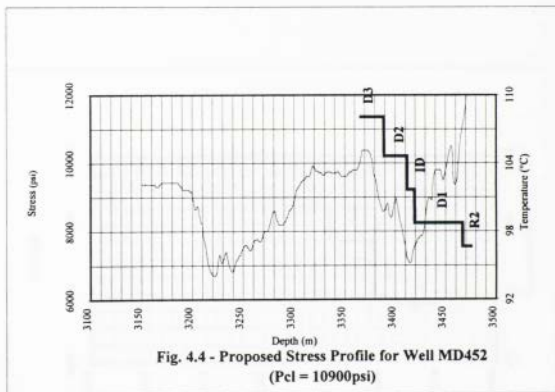
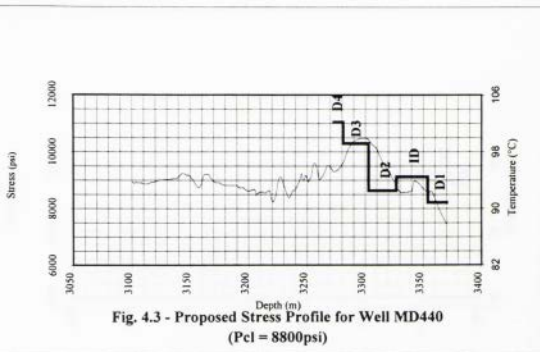
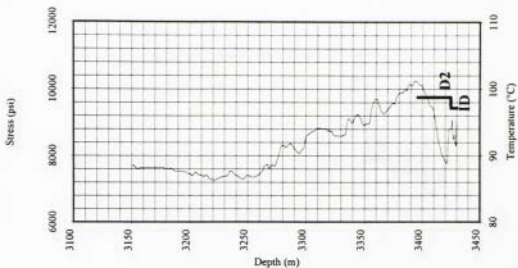
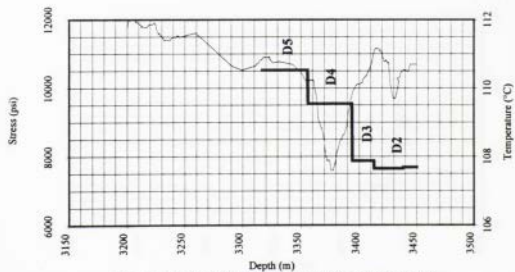


Fig. 4.2 - Proposed Stress Profile for Well Omn402
(Pcl = 8800psi)





**Fig. 4.5 - Proposed Stress Profile for Well Om1852
(Pcl = Uninterpreted)**



**Fig. 4.6 - Proposed Stress Profile for Well MD99
(Pcl = 8670 psi)**

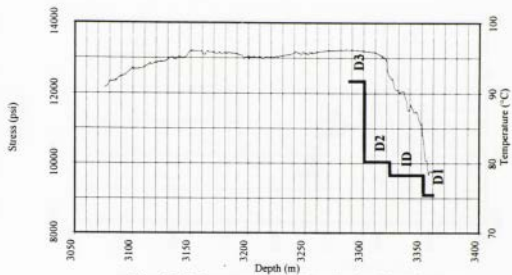


**Fig. 4.7 - Proposed Stress Profile for Well Omn541
(Pc1 = 7800 psi)**

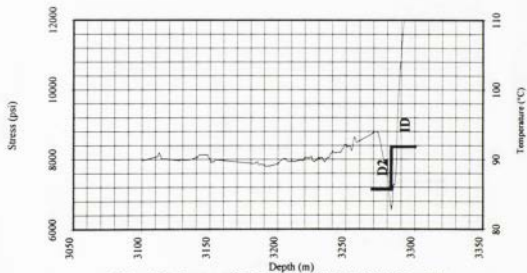


**Fig. 4.8 - Proposed Stress Profile for Well Omn70
(Pc1 = 9200 psi)**

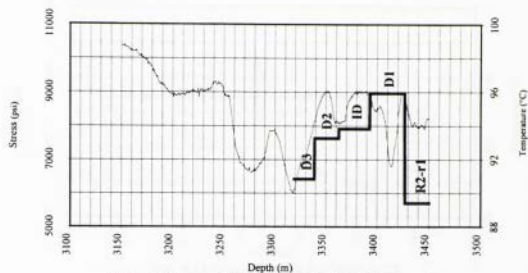


Fig. 4.9-Proposed Stress Profile for Well Omn84
(Pcl = 9430 psi)

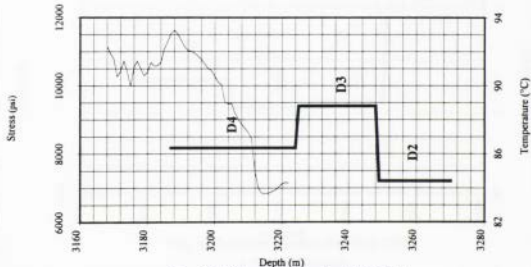


Fig. 4.10-Stress Profile for Well GS7
(Pcl = 8700 psi)

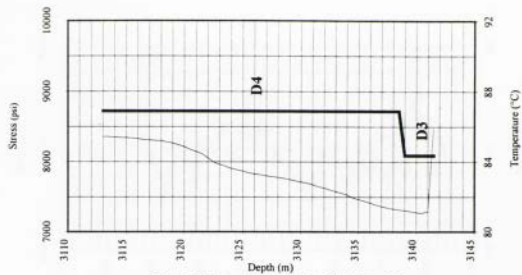


Fig. 4.11-Stress Profile for Well Ar22
(Pcl = 7600 psi)

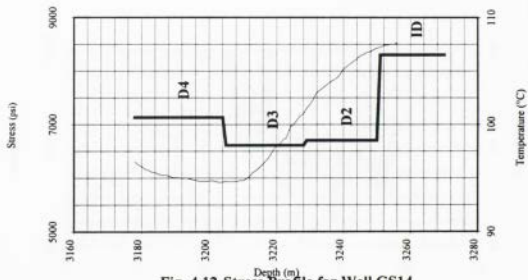
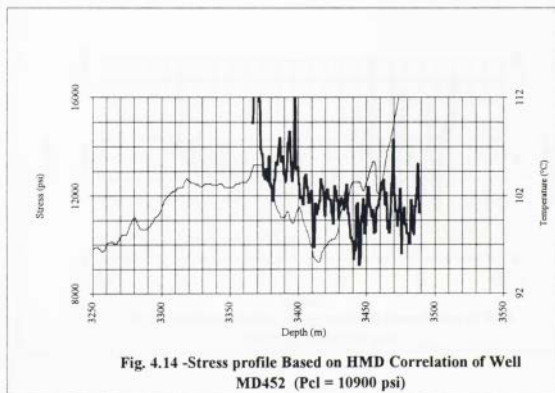
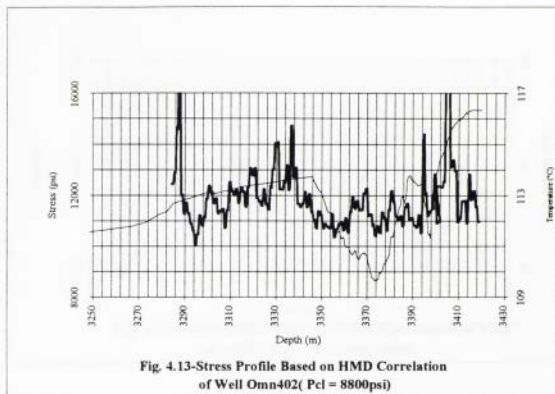


Fig. 4.12-Stress Profile for Well GS14
(Pcl = 6700 psi)



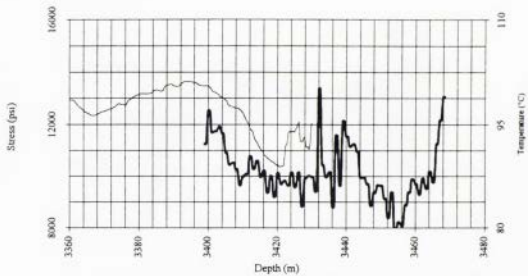


Fig. 4.15-Stress Profile Based on HMD Correlation of Well Oml852 (Pcl = Uninterpreted)

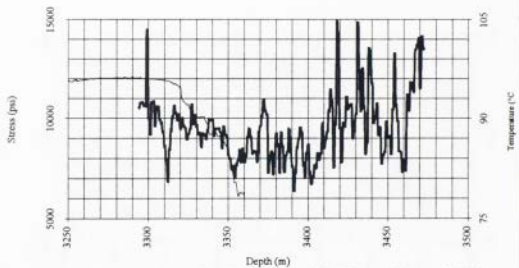
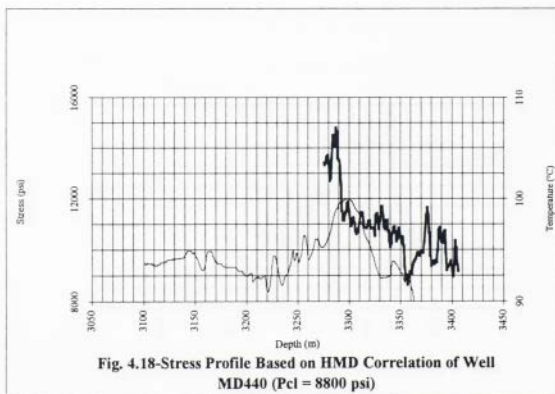
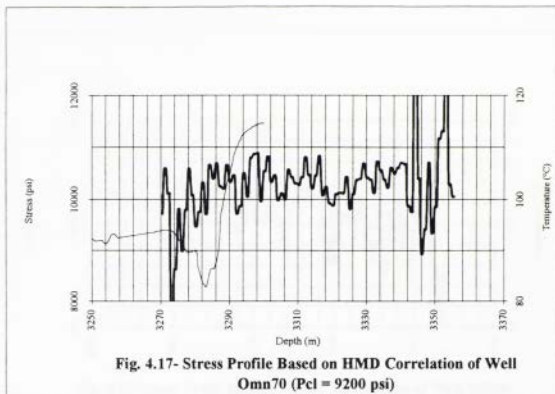
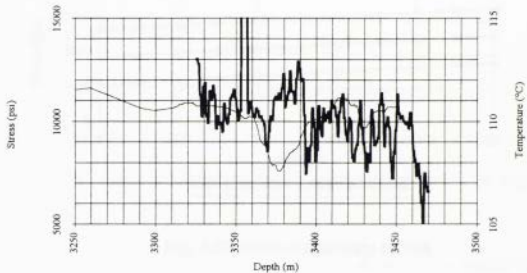
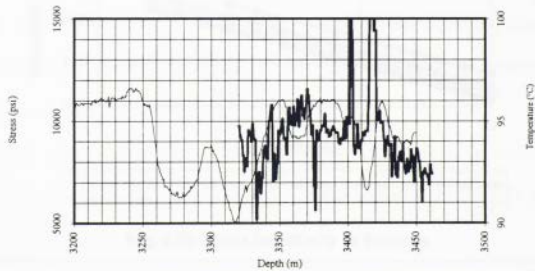


Fig. 4.16-Stress Profile Based on HMD Correlation of Well Omn541 (Pcl=7800 psi)





**Fig. 4.19-Stress Profile Based on HMD Correlation of Well MD99
(Pcl = 8670 psi)**



**Fig. 4.20-Stress Profile Based on HMD Correlation of Well
Omn84 (Pcl = 9430 psi)**

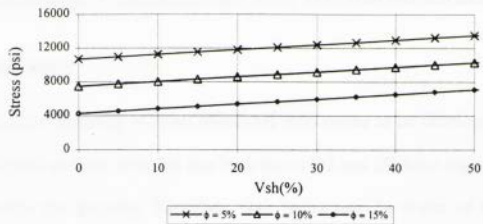


Fig. 4.21-Stress Sensitivity to Vsh

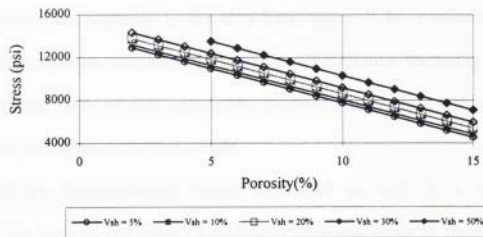


Fig. 4.22-Stress Sensitivity to Porosity

Chapter 5

Summary, Conclusions and Recommendations

5.1 Summary

Hydraulic fracturing in Hassi Messaoud field seems to be lithology dependent. Sedimentological analysis revealed that both layers D5 and D3 have high clay content associated with low porosity. Therefore, both layers may be drains of higher stress level.

Fracture containment in layered formations is believed to be mainly influenced by in-situ stresses and their distribution. A rigorous investigation of the in-situ stress field is the key to explaining the relationship between excessive treating pressures and fracture containment. Since no reliable theoretical formulation of stress profile exists, statistical correlation approach is the next best approach for predicting fracturing gradients. Such a correlation not only is crucial for hydraulic fracturing but also for drilling concerns such as lost circulation problems associated with unintentional fracturing due to inappropriate mud weight.

Based on microfracturing testing performed on well A, a stress profile correlation was obtained that relate the minimum horizontal stress to Young's modulus, E , and the oil saturation, S_o as follows:

$$\sigma_{h \min} = 6163.1 + 1312.2E - 74.416S_o \quad (3.2)$$

where:

$\sigma_{h \min}$ = minimum horizontal stress in *psi*,

E = Young's modulus in 10^6 *psi*, and,

S_o = the oil saturation expressed in %.

The dynamic Young's modulus was correlated with shaliness (V_{sh}) and porosity (ϕ_e) as follows:

$$E = 12.62 - 0.4318\phi_e - 0.0994V_{sh} \quad (3.1)$$

where:

E = Young's modulus in $10^6 psi$,

V_{sh} = the shale content in %, and

ϕ_e = the effective porosity in %.

Attempts to correlate minimum horizontal stress to elastic constants (Young's modulus E , Poisson's ratio ν , and $\nu/1-\nu$) in addition to shaliness (V_{sh}) alone were generally unsatisfactory. Nevertheless, a correlation was obtained between minimum horizontal stress ($\sigma_{h \min}$), shaliness (V_{sh}) and effective porosity (ϕ_e) as follows:

$$\sigma_{h \min} = 56.561V_{sh} - 642.358\phi_e + 13,886 \quad (3.7)$$

where:

$\sigma_{h \min}$ = minimum horizontal stress in psi ,

V_{sh} = shaliness in %, and

ϕ_e = the effective porosity in %.

The positive sign of V_{sh} shows that as the shaliness increases minimum horizontal stress increases. The negative sign of ϕ_e shows that as the porosity increases minimum horizontal stress decreases.

The application of the new obtained correlation leads to quite acceptable results: in wells Oml602, MD440, MD452, MD99, and MD439 the proposed correlation predicted

perfectly the location of the created fracture and the value of the minimum horizontal stress. In the other cases examined, the stress profile obtained based on the proposed correlation predicts the fracture location. Nevertheless it:

- Underestimates the stress value (case of Omn70 and Omn84)
- Overestimates the stress value (case of Omn541).

In both situations the difference is reduced considerably, relatively to the stress profile currently used. The obtained correlation was tested positively in two other fields;

- EL GASSI (wells GS7 and GS14).
- EL AGREB (well AR22).

The interpretation of wellbore breakouts reveals a very consistent direction for the maximum horizontal stress across Hassi Messaoud. Also, the stress orientation in Hassi Messaoud fits that observed in other locations in Algeria, where the orientation of the maximum principal stress is 135-140°azimuth, perpendicular to the principle faults and HMD anticline trends. This could be taken into account while selecting horizontal drilling azimuth planning.

The iso-fracturing gradient map confirms the compartmentalization of HMD structure into two compartments by the major fault ONI17 to MD395. The eastern compartment is more faulted and has the lowest fracturing gradient. The western compartment has the highest the fracturing gradient. This should be considered in selecting candidate wells for future hydraulic fracturing operations. It has been proven that occurrence of non-tip screen outs and production gain resulting from hydraulic fracturing treatments in Hassi Messaoud is function of the value of fracturing gradient. Indeed, the higher the fracturing gradient the higher the probability of occurrence of

non-tip screen outs and the more likely that production gain is low. Therefore, the eastern compartment is the one from where candidate wells for hydraulic fracturing are to be selected, with low fracturing gradients, bringing about higher probability of hydraulic fracturing treatment success. While the western compartment, where the fracturing gradients are higher, is where, statistically, hydraulic fracturing is less beneficial. Also, it is necessary to take into account, in the selection of candidate wells for hydraulic fracturing the proximity from a fault since such a discontinuity is thought to cause change in the orientation of a created fracture when it crosses it. Leading to high chances of bringing about a premature screen out while pumping the proppant into the fracture.

5.2 Conclusions

The main conclusions in this study are:

- 1- The stress profile in Hassi Messaoud could be correlated to shaliness and porosity
- 2- The correlation leads to acceptable results as long as porosity is $< 15\%$, and for a wide range of V_{sh} .
- 3- The maximum principal stress orientation in HMD field is $135-140^\circ$ azimuth.
- 4- The results of this work can be used in the selection of candidate wells for hydraulic fracturing.

5.3 Recommendations

For a more complete understanding of the mechanical aspect of Hassi Messaoud and its implications, thorough laboratory studies are recommended including:

- Elastic static and dynamic constant measurements must be made and then develop a correlation between them.
- Conduct measurements on oriented cores (ASR, DSCA, DWVA) to check the stress measurements already existing (magnitudes and orientation).
- Perform permeability measurements under conditions simulating the stress pathway in Hassi Messaoud.

Nomenclature

a	Conversion factor used in the calculation of the dynamic constants
B	Skempton's pore pressure coefficient
B_o and B_{oi}	Oil Formation factors at reservoir pressure and initial reservoir pressure
$C_{1, 2, 3, 4, 5, \& 6}$	Constants used in the equations for fracture length, maximum width, and injection pressure for constant injection rate
E	Young's modulus
E_d	Dynamic Young's modulus
E_S	Secant Young's modulus
E_t	Tangent Young's modulus
F	Force
G	Shear modulus
$G (\Delta t_D)$	G function
H	Height
HMD	Hassi Messaoud
K	Bulk modulus
K_{dd}	Dynamic drained bulk modulus
K_{du}	Dynamic undrained bulk modulus
K_{fr}	Bulk modulus of the rock framework
K_{lc}	Critical stress intensity factor
K_m	Mud bulk modulus
K_r	Bulk modulus of the solid grains
K_w	Water bulk modulus
P	Pressure
q_o	Injection rate
$R2$	Layer above R3
$R3$	Lower layer in HMD reservoir
Ra	Anisometric zone
Ri	Isometric zone
t	Time

t_c	Compressional transit time
t_s	Shear transit time
T_o	Tensile strength of the rock
V_{sh}	Shale volume
α	Biot coefficient
β	Bulk compressibility
Δ	Volumetric strain
ϵ_i	Component of strain
λ	Lamé's constant
μ	Lamé's constant
ν	Poisson's ratio
ν_d	Dynamic Poisson's ratio
ρ	Bulk density
σ	Stress
$\sigma_h, \sigma_H, \text{ \& } \sigma_V$	Principal stresses
$\sigma_r, \text{ \& } \sigma_\theta$	Radial and tangential stresses
$\sigma_1, \sigma_2, \text{ \& } \sigma_3$	Principal stresses
τ	Shear stress
ϕ	Porosity

References

1. Tiab, D., and Donaldson, E.C.: *Petrophysics*, Gulf Publishing Co, Houston, Texas, 1996.
2. Warpinski, N.R., Schmidt, R.A., and Northrop, D.A.: "In-situ Stresses: The Predominant Influence on Hydraulic Fracture Containment", *Soc. Pet. Eng. J.* (March 1982) 653-664.
3. Beghoul, M.S.: "Wellbore Geometry-Interpreting Ovalization", Well Evaluation Conference, HASSI MESSAOUD, Algeria 1995.
4. Djebbar, T.: "Fracture Estimation in Reservoirs", Well Evaluation Conference, HASSI MESSAOUD, Algeria 1995.
5. Hopkins, C.W.: "The Importance of In Situ Stress Profiles in Hydraulic Fracturing Applications". *J Pet Tech* (September 1997), 944-948.
6. Bellhaouas., R, Benani, A., and Despax, D.: "Improved Hydraulic Fracturing in Hassi Messaoud", Well Evaluation Conference, HASSI MESSAOUD, Algeria 1995.
7. Timur, A.: "Acoustic Logging", *Petroleum Engineering Handbook* 3rd edition, Society of Petroleum Engineers, Richardson, TX, 1992.
8. Van Terzaghi, K.: "Die berechnung der durchlassigkeitsziffer des tones aus dem verllauf der hydrodynamischen spannungerscheinungen", *SBER. Akad. Wiss.*, Wien, Vol. 132, 1923, pp. 105-113.
9. Biot, M. A.: "General theory of three dimensional consolidation.", *J. Appl. Phys.*, Vol. 12, 1941, pp. 155-164.
10. Cheng, C.H., and Johnston, D.H.: "Dynamic and Static Moduli" *Geophysical Research Letters*, vol. 8, N°.1, p 39-42, January 1981.
11. Yale, D.P. and Jamieson, W.H. Jr.: "Static and Dynamic Properties of Cabonates", *Rock Mechanics*, Nelson and Laubach (eds), 1994 Balkema, Rotterdam.
12. Hilbert, L.B., Hwong, Jr., T.K., Cook, N.G.W. Nihei K.T. and Myer, L.R: "Effects of Strain Amplitude on the Static and Dynamic Nonlinear Deformation of Berea Sandstone", *Rock Mechanics*, Nelson and Laubach (eds), 1994 Balkema, Rotterdam.

13. Mavko, G.M.: "Frictional Attenuation: An Inherent Amplitude Dependence", *Geophysics*, 1979, v. 84, pp. 4769-4775
14. Plona, T.J., and Cook, J.M.: "Effects of stress cycles on Static and Dynamic Young's Moduli in Castlegate Sandstone", *Rock Mechanics*, Daemen and Schultz (eds), 1995 Balkema, Rotterdam.
15. Tutuncu, A.N., Podio, A.L., and Sharma, M.M.: "Strain Amplitude and Stress Dependence of Static Moduli in Sandstones and Limestones". *Rock Mechanics*, Nelson and Laubach (eds), 1994 Balkema, Rotterdam.
16. Rahn, W.: "Stress Concentration Factors for the Interpretation of Door Stopper Stress Measurements in Anisotropic Rocks", *Intl. J. Rock Mech. Min. Sci. and geo. Abst.*, (1984), 21, N°6:313.
17. Roegiers, J.C., Vandamme, L.: "*Rock mechanics for the petroleum Engineer*", Note course of "Introduction To Rock Mechanics", PE 5133. Algeria. Summer 1997,
18. Smith, M.B.: "Effect of Fracture Azimuth on Production with Applications to the Watterburg Gas Field", paper SPE 8298 presented at the 1979 SPE Annual Technical Conference and Exhibition, Las Vegas, Sept. 23-26.
19. Dyes, A.B., Kemp, C.E., and Caudle, B.H.: "Effect of fractures on sweep-out Patterns", *J Pet Tech* (Oct. 1958) 245-49; *trans.*, AIME **213**.
20. Warpinski, N. R., Teufel, L.W.: "In-Situ Stresses in Low Permeability, Nonmarine Rocks", Paper SPE 16402 presented at the 1987 SPE/DOE Low Permeability Gas Reservoirs Symposium, Denver, May 18-19.
21. Teufel, L. W., Hart, C.M., Sattler, A. R., and Clark, J.A.: "Determination of Hydraulic Fracture Azimuth by Geophysical, Geological, and Oriented Core Methods at the Multiwell Experiment Site, Rifle, CO", Paper SPE 13226 presented at the 1984 SPE Annual Technical Conference and Exhibition, Texas, Sept 16-19.
22. Lacy, L.L.: "Comparison of Hydraulic-Fracture Orientation Techniques", Paper SPE 13225 presented at the 1984 SPE Annual Technical Conference and Exhibition, Houston, Sept 16-19.
23. Smith, M.B., Ren, N.-K., Sorrells, G.G., and Teufel, L.W.: "A Comprehensive fracture diagnostics Experiment: Part 2- Comparison of fracture Azimuth Measuring Procedures", Paper SPE 13894 presented at the 1985 SPE/DOE Low Permeability Gas Reservoirs Symposium, Denver, May 18-22.

24. Oikawa, Y., Matsunaga, I., Yamaguchi, T.: "Differential Strain Curve Analysis to Estimate the Stress State of the Hijiori Hot Dry Rock Field, Japan", *Intl. J. Rock Mech. Min. Sci. and geo. Abst.*, Vol. 30, N°7, pp. 1023-1026, 1993.
25. Matsuki, K., Takeuchi, K.: "Three Dimensional In Situ Stress Determination by Anelastic Strain Recovery of a Rock Core", *Intl. J. Rock Mech. Min. Sci. And geo. Abst.*, Vol. 30, N°7, 1993, pp. 1019-1022.
26. Ren, N.-K., and Hudson, P.J.: "Predicting the In situ State of Stress Using Differential Wave Velocity Analysis", 26th US Symposium on Rock Mechanics / Rapid City, SD / 26-28 June 1985.
27. Mc Lennan, J.D., and Roegiers, J.C.: "How Instantaneous are Instantaneous Shut-In Pressures?", Paper SPE 11064 presented at the 1982 SPE Annual Technical Conference and Exhibition, New Orleans, Sept 26-29.
28. Sarda, J.P., Perreau, P.J., Boutéca, M.J., Détienne, J.L. and Lassus-Dessus, J.: "Estimating Minimum In-Situ Stresses by Mean of Microfrac and Prefrac Testing", *Rock at Great Depth*, Maury and Fourmaintraux (eds), 1989 Balkema, Rotterdam.
29. Tinker, S.J., Baycroft, P.D., Ellis, R.C and Fitzhugh, E.: "Mini frac Tests and Bottomhole Treating Pressure Analysis Improve Design and Execution of Fracture Stimulations", Paper SPE 37431 presented at the 1997 SPE Production Operations Symposium, Oklahoma, March 9-11.
30. Proskin, S.A., Scott, J.D. and Chhina, H.S.: "Interpretation of the Minimum Principal Stress from Microfrac Tests", *Rock at Great Depth*, Maury and Fourmaintraux (eds), 1990 Balkema, Rotterdam.
31. Castillo, J.L.: "Modified Fracture Pressure Decline Analysis Including Pressure-Dependent Leakoff". Paper SPE 16417 presented at the 1987 SPE/DOE Low Permeability Gas Reservoirs Symposium, Denver, May 18-19.
32. Nolte .K.G. and Smith, M.B.: "Interpretation of Fracturing Pressures." paper SPE 8297 presented at the 1979 SPE Anual Technical Conference and Exhibition, Las vegas, Sept. 23-26.
33. Teufle, L.W.: "Prediction of Hydraulic Fracture Azimuth from Anelastic Strain Recovery Measurements of Oriented Core," *Proc.*, 23rd Symposium on Rock Mechanics: Issues in Rock Mechanics," R.E. Goodman and F.F. Hughes (eds), SME/AIME, New York City (1982) 239.
34. Warpinski, N.R., and Teufel, L.W.: "A Viscoelastic constitutive model for determining In-situ stress magnitudes from Anelastic Strain Recovery of core"

- Paper SPE 15368 presented at the 61st SPE Annual Technical Conference and Exhibition, New Orleans October, 5-8, 1986.
35. Shamir, G. and Zoback, M.D.: "The Stress Orientation Profile in the Cajon Pass, California, Scientific Drillhole, Based on Detailed Analysis of Stress Induced Borehole Breakouts", *Rock at Great Depth*, Maury and Fourmaintraux (eds), 1989 Balkema, Rotterdam.
 36. Vernik, L. and Zoback, M.D.: "Effects of Rock Elastic and Strength Properties in Estimation of Stress at Depth", *Rock at Great Depth*, Maury and Fourmaintraux (eds), 1989 Balkema, Rotterdam.
 37. Lee, M. and Haimson, B.: "Laboratory Study of Borehole Breakouts in Lac du bonnet Granite: a Case of Extensile Failure Mechanism", *Intl.J.Rock Mech.Min.Sci.andgeo. Abst*, Vol. 30, N^o.7, pp. 1039-1045, 1993.
 38. Seto, M., Utagawa, M., Katsuyama, K., Nag, D.K. and Vutukuri, V.S.: "In-situ Stress Determination by Acoustic Emission Technique", *Intl.J.Rock Mech.Min.Sci.andgeo*, 34: 3-4, paper N^o281, 1997.
 39. Michihiro, K., Fujiwara, T. and Yoshioka, H.: "study on estimating geostresses by the Kaiser effect of AE", 26th US Symposium on Rock Mechanics/rapid City, SD/26-28 June 1985.
 40. E. FJAER, et al.: *Petroleum Related Rock Mechanics*, ELSEVIER, 1992.
 41. Farquhar, R.A., Somerville, J.M., and Smart, B.G.D.: "Porosity as a Geomechanical Indicator: An Application of Core and Log Data and Rock Mechanics", Paper SPE 28853 presented at the European Petroleum Conference held in London, U.K., 25-27 October 1994.
 42. Sarda, J.P., Kessler, N., Wicquart, E., Hannaford, K. and Deflandre, J.P.: "Use of Porosity as a Strength Indicator for Sand Production Evaluation", Paper SPE 26454 presented at the 1993 SPE Annual Technical Conference and Exhibition, Houston, Texas, 3-6 October.
 43. Anderson, R. A., Ingram, D.S., and Zanier, A. M.: "Fracture Pressure Gradient Determination From Well Logs", *J. Pet. Tech.* (Nov. 1973) 1259-1268.
 44. Tixier, M. P., Morris, R.L., and Connell, J.G.: "Log Evaluation of Low Resistivity Pay sands in the Gulf Coasts," *Trans.*, SPWLA Ninth Annual Logging Symposium, New Orleans (June 1968).
 45. Cipolla, C.L., Liu, D. and Kyte, D.G.: " Practical application of In-situ Stress Profiles", Paper SPE 28607 presented at the 1994 SPE Annual Technical Conference and Exhibition, New Orleans, LA, U.S.A., 25-28 September 1994.

46. Whitehead, W.S., Hunt, E.R., Finley, R.J and Holditch, S.A.: "In-situ Stresses: A Comparison Between Log-Derived Values and Actual Field -Measured Values in the Travis Peak Formation of East Texas", Paper SPE 15209 presented at the Unconventional Gas technology Symposium of the SPE, Louisville, KY, May 18-21, 1986.
47. Morales, R.H.: "Microcomputer Analysis of Hydraulic Fracture Behavior with a Pseudo-Three-Dimensional Simulator," *SPEPE* (Feb. 1989) 69-74.
48. Woodland, D.C., and Bell, J.S.: "In-situ Stress Magnitudes from Minifrac Records in Western Canada", paper N80-39-67 presented at the 39th annual technical meeting of the petroleum society of CIM held in CALGARY, June 12-16, 1988.
49. Labudovic, V.: "How to Perform More Successful Fracturing of a Well", Paper SPE 10307 presented at the 58th SPE annual fall Technical Conference and exhibition held in San Antonio, Texas, October 5-7, 1981.
50. McGowen, J.M., Benani, A., Ziada, A.: "Increasing Oil Production by Hydraulic Fracturing in the Hassi Messaoud Cambrian Formation, Algeria". Paper SPE 36904 presented at the European Petroleum Conference held in Milan, Italy, 22-24 October 1996.
51. Daneshy, A.A.: "Experimental Investigation of Hydraulic Fracturing Through Perforations", Paper SPE 4333 presented at SPE-AIME European Spring Meeting held in London, U.K., 2-3 April 1973.
52. Internal Sonatrach Report, by: PED.
53. Internal Sonatrach Report, by: CRD.
54. Wright, C.A., Weijers, L., Germani, G.A., MacIvor, K.H., Wilson, M.K., and Whitman, B.A.: "Fracture Treatment Design and Evaluation in the Pakenham Field: A Reel- Data Approach", Paper SPE 36471 presented at the 1996 SPE Annual Technical Conference and Exhibition, Denver, Colorado, 6-9 October.
55. Internal Sonatrach report: "*Imagerie Ultrasonique en Découvert. Interprétation de l'ovalisation*" DP/HMD
56. Massa, D., Ruhland, M., and Thouvenin, J.: *Structure et Fracturation du Champ d'Hassi Messaoud (Algérie)*, éditions TECHNIP, Paris, 1972.

Appendix

Table A.1. Fracturing gradients in HMD

N	Well	frac gradient (psi/ft)
1	Md 9	1.03
2	Md 10	0.95
5	Md 43	0.97
6	Md 46	0.85
7	Md 53	0.88
8	Md 57	1.03
9	Md 59	0.82
10	Md 62	0.78
11	Md 64	0.91
12	Md 78	1.02
13	Md 99	0.87
16	Md 107	0.73
17	Md 109	0.83
18	Md 113	0.92
19	Md 114	0.81
22	Md 125	0.89
23	Md 128	0.92
24	Md 129	0.88
25	Md 130	0.71
26	Md 134	0.96
27	Md 138	0.91
28	Md 139	0.93
29	Md 140	0.89
30	Md 141	0.63
31	Md 149	0.85
32	Md 158	0.86
33	Md 164	0.81
34	Md 175	0.85
36	Md 179	0.86
37	Md 181	0.9
38	Md 189	0.74
39	Md 190	0.93
40	Md 192	0.85
42	Md 219	0.76
43	Md 221	0.99
46	Md 249	1.05
47	Md 251	0.98
48	Md 257	0.97
49	Md 258	1
50	Md 275	0.76
51	Md 279	1.05
52	Md 280	0.81
53	Md 283	1.04
54	Md 287	0.53
56	Md 299	1
57	Md 311	0.97

N	Well	frac gradient (psi/ft)
58	Md 316	0.97
59	Md 324	0.93
61	Md 340	0.76
62	Md 349	0.94
64	Md 361	1.05
67	Md 377	0.94
69	Md 387	0.86
72	Md 401	0.8
73	Md 407	0.8
74	Md 409	0.87
76	Md 417	0.99
77	Md 421	0.75
78	Md 437	0.84
79	Md 439	0.91
80	Md 440	0.86
81	Md 452	1.06
83	Om 6	0.92
84	Omk 16	0.81
85	Omk 35	0.87
86	Omk 102	0.82
87	Oml 11	0.86
88	Oml 30	0.84
89	Oml 31	0.89
90	Oml 82	0.68
92	Omm 66	0.92
93	Omm75	0.97
94	Omm 532	1.04
95	Omm 542	0.86
96	Omm 812	1.07
97	Omn 56B	0.84
98	Omn 70	0.91
99	Omn 84	0.9
101	Omn 243	0.85
102	Omn 332	1.04
104	Omn 402	1.03
105	Omn 541	0.87
106	Omn 653	0.94
107	Omn 702	0.93
109	Omo 42	0.92
110	Omo 751	0.78
111	Omo 852	0.88
112	Omp 11	0.77
113	Omp 16	0.7
114	Omp 31	0.75
115	Omp 33	0.86
116	Omp 42	0.76
117	Omp 143	0.65
118	Omp 712	0.73

Table A.2. to A.5 Average petrophysical parameter by layer (Zones: 1B, 17, 19, and 25)

Table A.2 Zone 1B

Layer	Shaliness	Porosity	Permeability
D5	12.9	5.9	2.04
D4	8.595	5.9	6.8
D3	14.8	6.9	2.59

Table A.3 Zone 17

Layer	Shaliness	Porosity	Permeability
D5	8.59	6.8	3.45
D4	5.76	8	15.45
D3	9.58	7.49	13.24
D2	7.45	8.82	42
ID	9.48	9.04	14.34
D1	10.68	10.66	33.08
R2-r1	14.15	12.7	24.44

Table A.4 Zone 19

Layer	Shaliness	Porosity	Permeability
D5	8.945	6.729	6.569
D4	7.33	4.74	4.36
D3	9.63	7.33	6.61
D2	7.437	7.473	17.812
ID	8.752	8.015	7.888
D1	10.327	8.946	11.271
R2-r1	20.751	13.08	2.73

Table A.5 Zone 25

Layer	Shaliness	Porosity	Permeability
D5	7.8	6.9	1.8
D4	8.067	4.2	4.00
D3	9.384	10.62	2.092
D2	8.992	9.602	15.031
ID	9.1	9.615	3.595
D1	11.943	10.72	3.68

Table A.6 summary of the data used in the correlation attempts

Layer	Stress	Poisson's Ratio (ν)	Young's modulus (E) psi	$\nu/(1-\nu)$	Vsh%	ϕ (%)
D5		0.1385	9244251	0.1607	39.93	
D4		0.0916	10594706	0.1009	13.49	
D3		0.1221	9153829	0.1391	19.49	
D2	11750	0.1024	10056365	0.1141	11.73	3.888
ID	12100	0.1205	8996501	0.137	11.57	5.74
D1	8450	0.1192	8280103	0.1354	8.52	8.44
Sandy Mound	9200	0.1031	8723019	0.115	14.637	5.03
R2-r1	9600	0.1722	7021269	0.208	23.97	8.87
R2-r2	11550	0.1307	6979280	0.1503	25.06	7.63
R3	10150	0.1628	6034942	0.1944	32.98	7.02
Oml602	7730	0.159	7001533	0.189	12.83	11.02
Md99	8670	-	-	-	4.29	7.32

Tables A.7 Stress estimation for the cited wells

Well Omn541 (Pcl=7800 psi and the fractured layers are D2 To Bottom)

	D3	D2	ID	D1	R2-r1	R2-r2	R3
Top	3288	3301	3323	3352	3381	3415	3463
Vsh	18.59	11.54	11.79	13.88	23.18	25.76	32.67
Porosity	4.05	7.00	7.62	8.69	9.67	8.74	7.95
Stress	12340	10040	9650	9090	8990	9730	10630

Well Om1602 (Pcl=7730psi and the fractured intervals are mainly R2 and the lower part of D1(3m))

	D1	R2
Top	3351	3373
Vsh	8.59	12.83
Porosity	9.93	11.02
Stress	7990	7530

Well Md440 (Pcl=8800psi and the fractured intervals are D2, ID & D1)

	D4	D3	D2	ID	D1	R2
Top	3273	3281	3303	3327	3354	3384
Vsh	6.57	6.96	2.28	5.62	5.35	8.18
Porosity	5.00	6.21	8.38	7.91	9.31	9.98
Stress	11040	10290	8630	9120	8210	7940

Well Omn70 (Pcl=9200psi and the fractured intervals are D2 & ID)

	D2	ID	D1	R2
Top	3269	3283	3310	3340
Vsh	1.07	2.82	3.66	16.21
Porosity	10.60	8.85	8.86	8.34
Stress	7130	8360	8400	9440

This volume is the property of the University of Oklahoma, but the literary rights of the author are a separate property and must be respected. Passages must not be copied or closely paraphrased without the previous written consent of the author. If the reader obtains any assistance from this volume, he must give proper credit in his own work.

I grant the University of Oklahoma Libraries permission to make a copy of my thesis upon the request of individuals or libraries. This permission is granted with the understanding that a copy will be provided for research purposes only, and that requestors will be informed of these restrictions.

NAME MAAMAR KOCEIR by ION ISPAS
DATE July 27 1999

A library which borrows this thesis for use by its patrons is expected to secure the signature of each user.

This thesis by MAAMAR KOCEIR has been used by the following persons, whose signatures attest their acceptance of the above restrictions.

NAME AND ADDRESS

DATE